Journal of Catalysis 263 (2009) 16–33

Contents lists available at ScienceDirect

Journal of Catalysis

www.elsevier.com/locate/jcat

Structural characterization of Ni–W hydrocracking catalysts using in situ EXAFS and HRTEM

S.D. Kelly [c], N. Yang [a,1], G.E. Mickelson [b], N. Greenlay [b], E. Karapetrova [a], W. Sinkler [b], Simon R. Bare [b,*]

[a] Argonne National Laboratory, Argonne, IL 60439, USA
[b] UOP LLC, Des Plaines, IL 60016, USA
[c] EXAFS Analysis, Bolingbrook, IL 60440, USA

ARTICLE INFO

Article history:
Received 25 September 2008
Revised 28 December 2008
Accepted 6 January 2009
Available online 24 February 2009

Keywords:
Hydrocracking
XAFS
XANES
HRTEM
In situ sulfidation
Nickel–tungsten sulfide

ABSTRACT

The detailed structural characterization of the metal function of two fully formulated Ni–W hydrocracking catalysts was investigated by time resolved in situ X-ray absorption spectroscopy (EXAFS and XANES) at both the Ni K-edge and W L_3-edge, and by high resolution transmission electron microscopy. These two hydrocracking catalysts (designated as HCA and HCB) contained the same wt% of Ni and W, the same wt% of the other constituents (γ-Al_2O_3/silico-aluminate), and were calcined at the same temperature, but were prepared by different methods in order to highlight the sensitivity of the characterization techniques to the structural differences. The morphology of the WS_2 particles in the sulfided catalyst is substantially different between the two catalysts: in the HCA catalyst there are many more particles with multiple WS_2 layers whereas in HCB there are more single layers. The average diameter of the WS_2 plates is similar in both. The catalysts show a difference in the amount of W sulfidation after the 410 °C sulfidation treatment in 10% H_2S/H_2. The W of HCA catalyst was completely sulfided whereas 16% W of HCB catalyst was unsulfided. Similarly there is a difference in the amount of sulfided Ni: 16% Ni in HCA and 60% Ni in HCB remain unsulfided. In the sulfided form of both catalysts the Ni exists in three different morphologies: oxidized Ni (six-fold coordinate as a nickel aluminate), nanoparticulate Ni_3S_2, and Ni decorating the edge sites of the WS_2. In both the Ni_3S_2, and Ni decorating the edge sites of the WS_2, the Ni is in a tetrahedral coordination with sulfur. In both catalysts the sulfidation of the Ni and W occurs essentially simultaneously over most of the temperature range and the sulfidation of the W proceeds through the same tungsten oxysulfide in both samples. The characterization methodology presented here is a powerful one for elucidating the structural differences of complex heterogeneous catalysts.

1. Introduction

Hydrocracking technology is an important conversion technology for producing high-value naphtha or distillate products from a wide range of refinery feedstocks. Supported Ni–W catalysts are very attractive in hydrotreating of heavy oil due to their high hydrogenation activity when the catalysts are sulfided [1–3]. The detailed characterization of the Ni–W family of catalysts has received far less attention in the literature than equivalent CoMo or NiMo catalysts. The hydrocracking catalysts are typically prepared from appropriate metal salts which are deposited onto the high surface area supports. Following a calcination step these metal salts form dispersed oxide phases which are then converted to the corresponding sulfides in a process known as sulfidation. It has been reported that Ni–W oxides in the precursor oxidic state are difficult to sulfide [4–6], and that the degree of sulfidation and the resulting structures that are formed strongly affect the catalytic performance [7]. It has also been shown that the difficulty of sulfidation of some relevant bulk compounds increases from $NiO > WO_3 > NiWO_4 > NiAl_2O_4$, and that the degree of sulfidation is strongly affected by the calcination temperature prior to the sulfidation: Increased calcination temperature results in Ni that is more difficult to sulfide [6]. Clearly many factors affect the degree of sulfidation of the Ni and W in this type of catalyst: the precursor salt used, the sulfidation temperature, the sulfidation pressure, the compound used for sulfidation, and the calcination temperature used prior to sulfidation, to name but a few.

The sulfidation of Ni–W/Al_2O_3 and W/Al_2O_3 catalysts has been studied using several different techniques including EXAFS, XANES, XPS, TEM, and temperature programmed sulfidation [8–12]. In addition to the studies on the alumina support, the sulfidation of carbon supported Ni–W catalysts has also been studied [13]. For tungsten-only catalysts there is only partial sulfidation of the tung-

* Corresponding author.
E-mail address: simon.bare@uop.com (S.R. Bare).
[1] Present address: Bruker AXS Inc., Madison, WI 53711, USA.

0021-9517/$ – see front matter
doi:10.1016/j.jcat.2009.01.019

sten by the typical final sulfidation temperature of 400 °C. This is also true for Ni–W catalysts supported on alumina. In one study it was estimated that only 50% of the W and 60% of the Ni is sulfided after sulfidation at 400 °C for 4 h at atmospheric pressure [10]. Fluorination of the alumina support aids the sulfidation of the Ni and W at lower temperatures and promotes the formation of the intermediate tungsten oxysulfide phases on the path to the final supported WS_2 phase. Catalysts prepared from ammonium tetrathiotungstate (ATT) as precursor (as opposed to the more usual ammonium metatungstate (AMT)) sulfide more readily than those prepared from AMT. An in situ EXAFS study showed a reduced contribution from W–O scattering in the final sulfided Ni–W catalysts compared to the AMT prepared catalyst [8]. It was interesting that W-only catalysts prepared from ATT resulted in the tungsten being fully sulfided, whereas the equivalent Ni–W catalyst contained a significant amount of oxidized W that was not sulfided, as determined from a W–O signal in the EXAFS spectra. Fluorination of the alumina in the ATT-prepared Ni–W/alumina catalyst increased the degree of sulfidation as only a small W–O contribution was observed by EXAFS. Using TEM it was shown that sulfided catalysts prepared from AMT contain mainly single layered slabs of WS_2, whereas those prepared from ATT comprise multi-layered slabs. The effect of the fluorination on the resulting structure of the WS_2 crystallites has also been studied [14]. It was concluded that the addition of fluoride produced larger and more stacked WS_2 crystallites.

The use of TEM to image the WS_2 layers, which appear as black "threads" in the images from platelets that are oriented "on-edge" on the support, has proven to be a powerful tool to study the morphology of the supported phase [15–18]. Recently the three-dimensional structure of the MoS_2 platelets in commercial Ni–Mo/γ-Al_2O_3 catalysts has been studied using electron tomography [19]. It was shown that the MoS_2 slabs form a complex interconnected structure within the alumina support, and that the shapes of the platelets deviate from those obtained using model systems [20]. There are also studies that show the occurrence of single layers are always under-reported when conventional TEM is used to image the sulfided particles [21].

EXAFS has proven to be a key technique in the study of Ni–W/γ-Al_2O_3 hydrocracking catalysts. However, in most cases even though there is both W and Ni in the catalyst only the W data are obtained and presented [22–25], presumably due to the complexity in fitting the Ni EXAFS data when multiple Ni-containing phases are present. The usual observation (and explanation) is a "W–S" signal at 2.41 Å and a "W–W" signal at 3.16 Å, due to the WS_2 platelets, and that the W–S and W–W coordination number are reduced from their bulk values due to the small sizes of the sheets. It has also been reported for these types of catalysts that the coordination numbers obtained by EXAFS do not agree with the expected values from the sizes visualized by TEM (see e.g. Ref. [23] for Ni–W, and Ref. [15] or MoS_2). For supported MoS_2 particles it was proposed that the reduced coordination numbers are due to structural and/or compositional distortion of the MoS_2 platelets [26].

Other studies have eschewed bulk sensitive characterization techniques and have focused on surface sensitive methods such as FTIR of chemisorbed NO, and XPS (see e.g. Ref. [27], and references therein). Using these methods Reinhoudt et al. [27] claimed that for an oxidic Ni–W/γ-Al_2O_3 catalyst four types of Ni were present: Ni as a surface aluminate, Ni in a mixed oxide with the W, Ni in a mixed oxide with W and Al, and bulk nickel aluminate.

There have also been studies conducted on planar model Ni–W catalysts [28]. In this work it was shown that the Ni converts rapidly to the sulfided state before the tungsten sulfides. However, when chelating agents, e.g. EDTA, were added the sulfidation of the Ni is retarded to higher temperatures such that the Ni and W sulfide in the same temperature range, leading to higher activity catalysts. It is believed that the metals should be sulfided simultaneously in order to obtain optimum interaction of the Ni and W, leading to formation of the more active Ni–W–S phase.

To the best of our knowledge there have been no detailed characterization studies of fully formulated Ni–W hydrocracking catalysts, i.e. containing a mixture of support phases. However, a recent study [29] describes the characterization of amorphous silica-alumina supported Ni–W catalysts. In this EXAFS/Mössbauer/TEM study it was shown that the initial partially sulfided Ni particles redisperse at a temperature that coincides with the onset of sulfidation of the tungsten. It was proposed that after sulfidation at 400 °C several Ni-containing phases were present: (i) Ni–W–S type structures, (ii) atomically dispersed nickel sulfide species present on the edges of the WS_2 particles, and (iii) small nickel sulfide species in close interaction with the partially sulfided tungsten oxysulfide species. It is noted that the researchers altered the Ni/W ratio for the EXAFS analysis of the Ni and W data in order to increase the signal-to-noise ratio at the Ni K-edge.

In the present paper, two different Ni–W hydrocracking catalysts samples (designated as hydrocracking catalyst A, HCA, and hydrocracking catalyst B, HCB) were characterized using in situ XAS, HRTEM and temperature programmed reduction. These catalysts are fully-formulated hydrocracking catalysts, containing not only the more usually studied γ-Al_2O_3 as support, but also silico-aluminate. Tungsten L_3-edge and nickel K-edge EXAFS data are presented that were recorded during both the in situ sulfidation at 410 °C in 10% H_2S/H_2, and on the fully sulfided catalysts after a four hour dwell at 410 °C. The in situ sulfidation pathway and relative sulfidibility of both the Ni and the W in the samples are compared. The local morphological differences of the samples in both the oxidic and sulfided state are discussed. The characterization methodology described in detail here exemplifies the detailed structural information that can be obtained on relatively complex catalysts, where the active metals are present in multiple phases. This is accomplished using a multi-shell EXAFS analysis combined in particular with electron microscopy. Structural differences between different catalysts are readily identified.

2. Experimental

2.1. Catalyst preparation

The catalysts were prepared using two different procedures. In both samples, the weight percentage of the two metals, Ni (from nitrate) and W (from ammonium metatungstate), is the same (with a Ni/W molar ratio of ∼unity), and the silico-aluminate supports have the same composition. The wt% tungsten in each catalyst is 1 wt%. The final calcination temperature is also the same for both catalysts. No complexing agents were used in the preparation. The sample made from the first method is named HCA and the one from the second method is named HCB.

2.2. Catalyst testing

The catalysts were tested for performance by using a hydrotreated light Arabian VGO doped with cyclohexylamine and di-*t*-butyl disulfide to provide 700 ppm of N and 2 wt% S, respectively. The pressure was 2000 psig and the feed rate 1.5 LHSV. Activity is represented by the temperature required for each catalyst to achieve 65 wt% net conversion of the feed to a cut point of less than 700 F. The testing was performed in a pilot plant optimized for yield differences.

2.3. Reference compounds

Tungsten sulfide, WS_2, was obtained from Aldrich, and the heazelwoodite (Ni_3S_2) was obtained from Cannon Microprobe. Both were checked for phase purity by powder XRD. Tungsten and nickel foils were obtained from EXAFS Materials Co. Nickel aluminate ($NiAl_2O_4$) was prepared by calcining stoichiometric amounts of nickel nitrate and gamma alumina and its structure confirmed by XRD.

2.4. Catalyst characterization

The samples were characterized by temperature programmed reduction, in situ EXAFS before, during and after sulfidation, and by transmission electron microscopy of the samples before and after sulfidation.

2.4.1. Temperature programmed reduction

The reducibility of the supported Ni and W metal oxides in the freshly prepared catalysts was investigated by temperature programmed reduction (TPR). Temperature programmed reduction was conducted using a custom built apparatus. A known concentration of hydrogen (5%) in argon gas is passed over a fixed amount of sample (250 mg) in a quartz reactor while the temperature is increased at a linear rate. Downstream of the reactor the water in the gas phase is trapped before the effluent is sent to a thermal conductivity detector. The difference in hydrogen concentration before, during and after reduction is measured. The apparatus is calibrated using a series of five injections through a fixed sample loop (0.2 cm^3) of 100% hydrogen before each experiment to obtain quantitative data on the extent of reduction of metal oxide(s) at the selected temperatures.

2.4.2. In situ XAFS measurements

The W L_3- and Ni K-edge XAFS spectra of the catalyst and reference samples were collected at the 33 BM beamline at the Advanced Photon Source (APS), Argonne National Laboratory. The storage ring of APS was operated at 7 GeV with a constant ring current of 105 mA. A double crystal monochromator with Si(111) crystals was used to select the incident X-ray energy. Harmonics were removed by two Rh-coated mirrors, with the first mirror also acting as a collimator.

X-ray absorption spectra were collected during in situ temperature programmed reduction and during in situ temperature programmed sulfidation. The XANES spectra of the Ni and W were measured on different samples of each catalyst during the reduction in a flow of 20% H_2/He at the same ramp rate as the TPR measurements (5 deg/min).

The in situ EXAFS temperature programmed sulfidation was carried out using a custom-designed in situ reactor described in detail elsewhere [30]. The extrudate sample was ground and diluted with BN powder to give a sample of appropriate absorption length. Approximately 250 mg of the mixture was pressed into the 10 mm ID quartz sample holder. The weight of the sample was calculated to have a total absorption length of about 2.0, and the fractional absorption by W or Ni of approximately 0.5. Initially, EXAFS data of the as-received, oxidized (calcined) sample were collected. The catalysts were then in situ sulfided by incremental heating at 4 °C/min to 410 °C in a flow of 10% H_2S/90% H_2 at a pressure of 1 bar, followed by a dwell at 410 °C for 4 h. In situ EXAFS data were collected during the temperature ramp. Due to the finite time required to collect each scan (approximately 10 min) the temperature differential between the first and last point in each scan is about 40 °C. The temperature at the absorption edge is indicated in figures. After the ramp and hold in H_2S/H_2 the sample was cooled to around 70 °C in the gas mixture before purging with pure helium. Multiple EXAFS spectra of the sulfided catalysts were collected and averaged in order to improve the signal/noise ratio.

2.4.3. TEM measurements

The samples for TEM were prepared by lightly grinding and dispersing in isopropanol. Microscopy was performed on a JEOL 3010 TEM equipped with an ultra-high-resolution pole piece (C_s of 0.6 mm), operated at 300 kV.

2.5. Data analysis

2.5.1. XANES analysis

The relative amount of unreduced to reduced Ni and W in the catalysts as a function of temperature is obtained from the XANES spectra using linear combination fitting. Each spectrum was fit to a linear combination of the measured initial oxidic spectrum of each catalyst and the corresponding metal foil (as representative of the metallic contribution in each). These fits assume that only two species of Ni and W are present: an oxidized species and a reduced (metallic species). This is clearly a gross oversimplification, and neglects any intermediate phases that may be present during the reduction. Nevertheless, the linear combination fits that are obtained using this method are visually similar to the measured spectrum as determined by the small residual. This method is used only as a guide to the reducibility of each metal.

The percentage of sulfidation of the Ni and W in each sample as a function of temperature is determined by using a linear component fit to the XANES spectra. Each spectrum was fit to a linear combination of the measured initial oxidic spectrum of each catalyst and the measured spectrum of bulk WS_2 (for the W XANES data) or Ni_3S_2 (for the Ni XANES data). Similar to the TPR-XANES fitting the fitting of the sulfidation XANES data neglect any intermediate species that may be present. Nevertheless, this methodology is a useful guide to the ease of sulfidation of the metals on the two catalysts.

2.5.2. EXAFS analysis

EXAFS data reduction and analysis were performed using Athena [31], which is an interface to IFEFFIT [32] and FEFFIT [33]. The background was removed from each data set, and then the resulting $\chi(k)$ data were averaged using standard procedures. The Fourier transforms of the measured spectra were modeled with a k-weight of 1, 2, and 3. The Fourier transform (FT) figures are shown with the data processed with a k-weight of 3. The theoretical models were constructed from FEFF [34] based on the crystal structures of WS_2 [35] and Ni_3S_2 [36] for the sulfided catalysts and from WO_2 [37] and $NiAl_2O_4$ [38] for the oxidized components. The FT spectra are shown without phase correction. The parameters determined from the EXAFS spectra include an amplitude reduction factor (S_0^2), coordination number (CN), change in atom pair length (ΔR), mean square displacement of the atom pair length (σ^2) and change in E_0 (ΔE_0). The disorder term σ^2 contains both structural and static disorder in the distance between the atom pairs.

The EXAFS data from the bulk WS_2 standard was Fourier transformed over the data range from 3.0 to 16.0 $Å^{-1}$ and modeled within the region from 1 to 6.5 Å. This data and modeled regions contain approximately 47 independent points [39]. The EXAFS model based on the crystal structure of WS_2 contains 10 parameters; an S_0^2-value, an energy-shift value, two parameters that depend on the unit cell, and 6 σ^2 values. This is a well constrained model because the number of independent points is 4.7 times more than the number of parameters determined in the model. The EXAFS parameterization and best-fit values for WS_2 standard are listed in Table 1. R_{eff} is the initial reference half

Table 1
W L_3-edge EXAFS parameterization and best-fit values for WS_2 standard.

Path	CN	R_{eff} (Å)	R (Å)	Parameterization of σ^2	σ^2 ($\times 10^{-3}$ Å^2)
W–S_1	6	2.477	2.398 ± 0.003	$\sigma^2_{(S_1)}$	2.4 ± 0.4
W–W_1	6	3.154	3.160 ± 0.002	$\sigma^2_{(W_1)}$	2.7 ± 0.2
W–S_2	6	4.011	3.967 ± 0.003	$\sigma^2_{(S_2)}$	4.5 ± 1.3
W–W_1–S_1	24	4.054	3.978 ± 0.004	$\sigma^2_{(W_1)}$	2.7 ± 0.2
W–S_2–W_1	24	4.821	4.762 ± 0.004	$\sigma^2_{(S_2)}$	4.5 ± 1.3
W–S_4	12	5.102	5.072 ± 0.004	$\sigma^2_{(S_4)}$	21.7 ± 10.0
W–S_4–W_1	24	5.367	5.315 ± 0.004	$\sigma^2_{(S_4)}$	21.7 ± 10.0
W–S_4–S_2	24	5.367	5.315 ± 0.004	$\sigma^2_{(S_4)}$	21.7 ± 10.0
W–W_2	6	5.463	5.473 ± 0.004	$\sigma^2_{(W_2)}$	3.8 ± 1.1
W–S_5	12	5.496	5.601 ± 0.004	$\sigma^2_{(S_4)}$	21.7 ± 10.0
W–W_1–S_4–S_1	24	5.631	5.558 ± 0.004	$\sigma^2_{(S_4)}$	21.7 ± 10.0
W–S_5–S_1	24	5.665	5.784 ± 0.004	$\sigma^2_{(S_4)}$	21.7 ± 10.0
W–W_1–W_2	24	5.885	5.897 ± 0.004	$\sigma^2_{(W_2)}$	3.8 ± 1.1
W–W_3	6	6.308	6.320 ± 0.005	$\sigma^2_{(W_3)}$	4.3 ± 0.7
W–W_1–W_3	12	6.308	6.320 ± 0.005	$\sigma^2_{(W_3)}$	4.3 ± 0.7
W–W_{1a}–W–W_{1b}	6	6.308	6.320 ± 0.005	$2 \times \sigma^2_{(W_1)}$	5.4 ± 0.4
W–W_1–W_3–W_1	6	6.308	6.320 ± 0.005	$\sigma^2_{(W_3)}$	4.3 ± 0.7
W–S_1–W–S_2	12	6.488	6.365 ± 0.006	$2 \times \sigma^2_{(S_2)}$	9.0 ± 2.6
W–S_6–W_1	12	6.777	6.760 ± 0.005	$\sigma^2_{(S_4)}$	21.7 ± 10.0
W–S_4–W_3–W_1–W_1	24	6.944	6.895 ± 0.005	$\sigma^2_{(W_3)}$	4.3 ± 0.7
W–S_6–W_1–W_1	24	6.971	6.943 ± 0.005	$\sigma^2_{(S_4)}$	21.7 ± 10.0

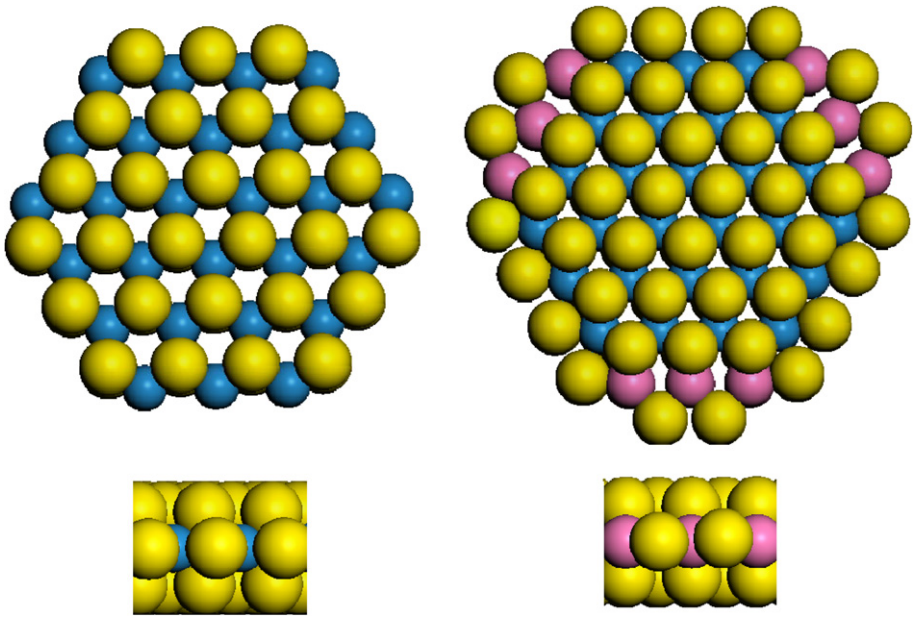

Fig. 1. Plan view (left) and side view (bottom left) of a small cluster with the bulk WS_2 structure. Each tungsten atom (blue) is 6-fold coordinate with sulfur (yellow). Plan view (right) and side view (bottom right) of a small WS_2 cluster with the Ni atoms (magenta) 4-fold coordinated on the $(10\bar{1}0)$ edge of the WS_2 cluster.

path length as determined previously from XRD as obtained from the Inorganic Crystal Structure Database, ICSD. The EXAFS half path length was parameterized in terms of the crystallographic structure of WS_2. The unit cell dimensions are $a = b = 3.1540$ Å, $c = 12.360$ Å, and the position of the sulfur atom within the unit cell in the z-direction (S_z) is given by the fractional offset of 0.1140. The unit cell dimension, c, could not be determined accurately due to the very small signal from adjacent atomic planes in the z-direction. Therefore this value was held at the crystallographic position. The intraplanar distance, $a = b$, was optimized to the value 3.160 ± 0.002 Å with a S_z value of 0.1240 ± 0.0004. The EXAFS best-fit values for the half path lengths (R) are listed in Table 1. σ^2 is parameterized in terms of 6 unique values. The best-fit values for σ^2 are also listed. An energy shift value of -3.4 ± 0.4 eV and an S_0^2 value of 0.87 ± 0.04 were also determined in the fit to the measured spectrum.

The W L_3-edge EXAFS model for the sulfided forms of the HCA and HCB samples was based on the EXAFS model of the WS_2 standard. Fig. 1 and Fig. S2 show a schematic of the layered WS_2 structure. The amplitude of the measured EXAFS spectra from HCA/B are less than that of the WS_2 standard (see Fig. 12), therefore many of the small multiple scattering paths needed to characterize the standard do not contribute significantly to the HCA and HCB spectra. The simplified path list and the parameterization of the model for HCA and HCB are listed in Table 2. The EXAFS data from the samples were Fourier transformed over the data range from 3.0 to 16.0 Å^{-1} and modeled within the region from 1 to 6.3 Å. This data and modeled regions contain approximately 46 in-

Table 2
W L_3-edge EXAFS parameterization and best-fit values for HCA and HCB spectra.

Path	Bulk CN	Best-fit CN	R_{eff} (Å)	R (Å)	Parameterization of σ^2	σ^2 ($\times 10^{-3}$ Å^2)
			HCA			
W–S_1	6	5.7 ± 0.2	2.477	2.402 ± 0.002	$\sigma^2_{(S_1)}$	2.9 ± 0.3
W–W_1	6	3.6 ± 0.4	3.154	3.159 ± 0.003	$\sigma^2_{(W_1)}$	4.1 ± 0.5
W–S_2	6	3.6 ± 0.4	4.011	3.968 ± 0.003	$\sigma^2_{(S_2)}$	6.0 ± 2.1
W–W_2	6	4.4 ± 3.1	5.463	5.471 ± 0.006	$\sigma^2_{(W_2)}$	7.7 ± 3.4
W–W_3	6	7.7 ± 4.0	6.308	6.317 ± 0.007	$\sigma^2_{(W_2)}$	7.7 ± 3.4
W–W_1–W_3	12	7.7 ± 4.0	6.308	6.317 ± 0.007	$\sigma^2_{(W_2)}$	7.7 ± 3.4
			HCB			
W–O_1	6	0.9 ± 0.1	1.95–2.06	1.82 ± 0.02	$\sigma^2_{(S_1)}$	8.8 ± 3.8
W–S_1	6	5.1 ± 0.1	2.477	2.400 ± 0.002	$\sigma^2_{(W_1)}$	3.2 ± 0.3
W–W_1	6	3.2 ± 0.3	3.154	3.158 ± 0.003	$\sigma^2_{(S_2)}$	4.1 ± 0.5
W–S_2	6	3.2 ± 0.3	4.011	3.966 ± 0.003	$\sigma^2_{(W_2)}$	6.7 ± 2.0
W–W_2	6	3.6 ± 2.3	5.463	5.470 ± 0.006	$\sigma^2_{(W_2)}$	7.5 ± 3.1
W–W_3	6	6.7 ± 3.1	6.308	6.316 ± 0.006	$\sigma^2_{(W_2)}$	7.5 ± 3.1
W–W_1–W_3	12	6.7 ± 3.1	6.308	6.316 ± 0.006	$\sigma^2_{(S_1)}$	7.5 ± 3.1

dependent points [39]. The resulting EXAFS model, based on the crystal structure of WS_2, contains 11 parameters; 4 coordination number (CN) values, an energy-shift value, two parameters that depend on the unit cell, and 4 σ^2 values. The S_0^2 value was held at 0.87 ± 0.04 and the uncertainty is propagated in quadrature to the CN values. This is a well-constrained model because the number of independent points is more than 4 times the number of parameters determined in the model.

If all the W atoms within the HCA and HCB samples are within the WS_2 sheets, the best-fit value for the number of near neighbor S atoms should be close to 6. Even if the average particle size (diameter) of the WS_2 sheets is small the W atoms on the edges of the sheet will still be 6 fold coordinated with S atoms. The best-fit value for the first neighboring S atoms for the HCA and HCB samples were determined to be 5.7 ± 0.2 and 5.1 ± 0.1, respectively. The coordination number of the HCA sample is close to the expected value of 6 while that of the HCB sample is significantly less indicating that the W is under-coordinated with S atoms. To explain this small CN for the HCB sample, a tungsten-oxygen (W–O_1) contribution was added to the model representing an oxidic component. The W in WO_2 is 6-fold coordinated with oxygen with bond length distances of 1.95 to 2.06 Å. Therefore the first shell coordination numbers were constrained to have a total of 6 O and S atoms with the percentage of each determined by the measured spectra [i.e. CN(W–S_1) = fraction × 6, and CN(W–O_1) = (1 − fraction) × 6]. The reduced-chi-square value, a quality of fit metric, decreased by 40% after including the oxide component. A standard deviation in the reduced-chi-square value is a change by 25%. Therefore the inclusion of the W–O_1 signal is a statistically valid improvement for the HCB spectra. This model was also applied to the HCA spectra but the resulting 10% improvement of the reduced-chi-square value led to the conclusion that the W–O_1 contribution to the HCA sample was insignificant.

The particle size (and theoretically shape) of the dispersed WS_2 can be determined from the average coordination numbers for the EXAFS paths beyond the first W–S path. As the WS_2 platelet size becomes smaller the number of W–W scattering paths will decrease as the W atoms on the exterior of the layer will be under-coordinated (have fewer neighboring atoms since they are on the edge of the particles), and the average W–W coordination for all W atoms within the particles decreases. For example tungsten in WS_2 has six tungsten atoms with a bond length of 3.15 Å. If the particles become so small that half the W neighbors are on the edge surface then these surface W atoms have only 3 W neighbors. Thus the average coordination number determined from the EXAFS spectra will be the weighted average of 4.5 W neighbors.

Table 3
EXAFS parameterization for the Ni K-edge of the oxidized HCA, oxidized HCB, sulfided HCA and HCB catalysts.

Path	Path description		EXAFS parameters			
	CN	R (Å)	CN	ΔR (Å)	σ^2 (Å^2)	ΔE (eV)
			Paths for Ni–WS_2			
Ni–S_1	2	2.23	F(S)·4	ΔR_S	$\sigma^2_{S_1}$	ΔE_1
			Paths for nanoparticulate Ni_3S_2			
Ni–S_1	2	2.23	F(Ni_3S_2)·2	$\alpha_{Ni_3S_2}$·2.23	$\sigma^2_{S_1}$	ΔE_1
	2	2.26	F(Ni_3S_2)·2	$\alpha_{Ni_3S_2}$·2.26	$\sigma^2_{S_1}$	ΔE_1
Ni–Ni_1	2	2.48	F(Ni_3S_2)·2	$\alpha_{Ni_3S_2}$·2.48	$\sigma^2_{Ni_1}$	ΔE_1
	2	2.50	F(Ni_3S_2)·2	$\alpha_{Ni_3S_2}$·2.50	$\sigma^2_{Ni_1}$	ΔE_1
			Paths for $NiAl_2O_4$[a]			
Ni–O_1	6	1.97	F($NiAl_2O_4$)·6	ΔR_{O_1}	$\sigma^2_{O_1}$	ΔE_1
Ni–Ni_1	3	2.85	F($NiAl_2O_4$)·3	ΔR_{Ni_1}	$\sigma^2_{Ni_1}$	ΔE_1
Ni-Al_1	3	2.85	F($NiAl_2O_4$)·3	ΔR_{Al_1}	$\sigma^2_{Al_1}$	ΔE_1
Ni-Al_2	6	3.34	F($NiAl_2O_4$)·6	ΔR_{Al_2}	$\sigma^2_{Al_2}$	ΔE_1
Ni–O_2	6	3.51	F($NiAl_2O_4$)·6	ΔR_{O_2}	$\sigma^2_{O_2}$	ΔE_1
Ni–O_3	12	4.48	F($NiAl_2O_4$)·12	ΔR_{O_3}	σ^2_{O3}	ΔE_1
Ni–O_4	12	4.55	F($NiAl_2O_4$)·12	ΔR_{O_3}	$\sigma^2_{O_3}$	ΔE_1
Ni–Ni_2	6	4.93	F($NiAl_2O_4$)·6	ΔR_{Ni_2}	$\sigma^2_{Ni_2}$	ΔE_1

[a] Model for oxidized catalyst with F($NiAl_2O_4$) = 1.

The Ni amplitude reduction factor, S_0^2, was determined from the EXAFS spectrum of Ni foil. The model determines S_0^2, one energy shift parameter for all paths, 4 Debye temperatures through which the σ^2 values were determined, and an expansion/contraction term (α) for all path lengths. The model contains 7 parameters. The data range was from 2.5 to 13 Å^{-1} and the fit range was from 1.4 to 5 Å. The model was well constrained by the 26 independent points of the data. An energy shift value of -2.7 ± 0.6 eV, an S_0^2 value of 0.92 ± 0.06, and α of $0.2 \pm 0.1\%$ were determined in the fit to the measured spectrum.

The Ni EXAFS spectra from the oxidized HCA/B catalysts can be accurately described by a model based on the $NiAl_2O_4$ structure with all the Ni in the octahedral sites of the spinel. This simple one oxygen shell model applied to the oxidized HCA and HCB catalysts gives an O CN of 6.0 ± 0.3 and 5.8 ± 0.3, respectively. This simple test indicates that the vast majority of the Ni in the oxidized

catalysis is in an octahedral site (6-fold coordinate). The model for $NiAl_2O_4$ is described in the third section of Table 3 and contains several O, Ni and Al paths. Each path is described by ΔR and σ^2 terms resulting in 14 variables. The model also includes one energy shift parameter for a total of 15 variables. The data range is from 3 to 11 $Å^{-1}$ and the fit range is from 1 to 5 Å, resulting in 22 independent points in the modeled spectrum. The Ni K-edge EXAFS data of the oxidized HCA catalyst was simultaneously modeled with the Ni K-edge EXAFS spectrum of the HCA after 4 h at 410 °C in the flow of H_2S/H_2 (sulfided HCA), and similarly for HCB, as explained below.

Initially, the Ni EXAFS data of sulfided HCA and sulfided HCB samples were modeled with one sulfur shell. The CN for the S shell is 3.9 ± 0.4 and 3.9 ± 0.5 for the sulfided-HCA and sulfided-HCB spectra, respectively. These results are consistent with the expectation that the sulfided Ni atoms decorate the edges of the WS_2 sheets with two S atom shared with the sheet and two S atom not bound to the sheet, as for model Co–Mo–S or Ni–Mo–S catalysts [20], but is different from prior EXAFS work on supported Ni–W–S catalysts [8,13]. This model does not, however, explain all the EXAFS spectra, nor is it consistent with the XANES spectra that indicate some remaining oxidized Ni in the sulfided HCB sample. Therefore, the sulfided HCA and oxidized HCA were simultaneously modeled. The oxidized spectrum was used to describe a residual oxidic component in the sulfided-HCA/B samples. This was done by determining a scaling factor $F(NiAl_2O_4)$ for the sulfided-HCA/B samples as shown in Table 3. This model was further refined by the addition of a separate nanoparticulate Ni_3S_2 phase. This Ni_3S_2 phase represents a small cluster of Ni atoms tetrahedrally-coordinated by sulfur either on the edges of the WS_2 sheets or elsewhere on the support (see discussion, below). The addition of a Ni–Ni scattering path in this phase significantly increased with quality of the fit in the region from 1.0 to 2.6 Å with a decrease in the χ^2_η (as calculated by $\chi^2_{\eta i}/\chi^2_{\eta f} - 1$) of 1.3 (two standard deviations are 1.1). The model including the three different phases of Ni is described in Table 3. The percentage of the three phases was constrained to be 100%. Hence the amount of nanoparticulate Ni_3S_2 [$F(Ni_3S_2)$] was determined from the amount of mono-atomic Ni decorating the edges of WS_2 [F(S)] and the amount of oxidized Ni [$F(NiAl_2O_4)$]. The nanoparticulate clusters of Ni_3S_2 are represented by 4 S atoms and 4 Ni atoms as determined from the crystalline structure of Ni_3S_2. The distances to these neighboring atoms were constrained in terms of an expansion/contraction term ($\alpha_{Ni_3S_2}$). The model for the sulfided-HCA/B samples includes 7 parameters, listed in Table 3, along with the 15 parameters described above for the oxidized catalysts. The model was simultaneously refined to the sulfided-HCA and oxidized-HCA spectra and also to the sulfided-HCB and oxidized-HCB spectra. The sulfided-HCA/B spectra were Fourier transformed from 3.2 to 12 $Å^{-1}$ and modeled from 1 to 5 Å, giving a 24 independent points in each of the modeled spectra.

2.5.3. TEM analysis

An analysis of the TEM images of the two sulfided samples was performed to determine the length and the number of WS_2 layers from a large number of individual particles. For each sample several images were used with typically ten to several tens of particles per image. Thicker regions of the images, which have limited interpretability, were not analyzed. The analysis was performed using a script program in which a particle is selected, its length determined by keying locations at both ends, and the number of layers in the particle assessed visually and entered by hand. Assuming that the true WS_2 particle shape can be approximated as circular when viewed along the crystallographic *c*-axis, the available area at the particle edge is proportional to the number of layers n times the circumference πd, where d is the length of the particle measured from the image. The length-weighted stack number given by

$$\bar{n} = \frac{\sum_i n_i d_i}{\sum_i d_i}.$$

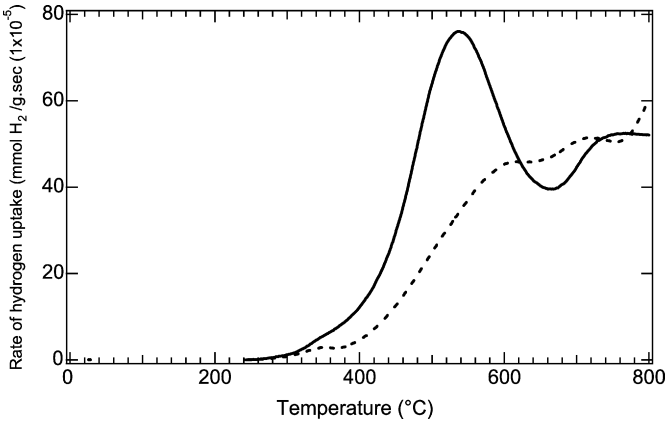

Fig. 2. Temperature programmed reduction (TPR) of HCA (solid) and HCB (dashed).

3. Results

3.1. Catalyst activity

Averaged over several experimental runs the distillate yield (defined as the 300–700 °F range) of HCB is always 2–3 degrees lower than HCA. Clearly then the method of sample preparation has an effect on the performance of the catalyst.

3.2. Determination of S_0^2

The S_0^2 for W based on WS_2 and for Ni based on Ni foil was determined as 0.87 ± 0.04 and 0.92 ± 0.06, respectively. These values were used to model the Ni and W EXAFS spectra from the HCA and HCB catalysts.

3.3. Reducibility of catalysts: TPR

The reducibility of the supported Ni and W oxidic phases in the freshly prepared (calcined) catalysts was investigated by temperature programmed reduction (TPR) and in situ TPR-XANES. A comparison of the reducibility, as measured by the rate of hydrogen uptake, of the two samples is shown in Fig. 2. The data indicate that the W and Ni in the oxidized catalysts are more reducible (indicated by the integrated area under the rate of hydrogen uptake curves) in the catalyst HCA versus HCB. However, TPR cannot differentiate whether it is the Ni or W (or both) that is reducing as only the total hydrogen uptake is measured. In order to determine which metal (Ni or W) is reducing at what temperature, the same samples were studied using in situ XANES measurements during temperature programmed reduction, where the XANES spectra of the Ni and W were measured separately during the reduction. These TPR-XANES spectra are shown in Fig. 3. The resulting amount of the metallic component in each spectrum based on linear combination fitting of the XANES spectra as a function of temperature is shown in Fig. 4.

By 600 °C ~80% of the Ni in HCA is reduced whereas in HCB less than 60% of the Ni is reduced. There is little measurable reduction of the tungsten by 600 °C in either of the catalysts. In HCA the tungsten oxide species are just starting to reduce by this temperature, whereas in the HCB there is virtually no reduction of the tungsten by 600 °C. Thus, by combining the element-specific

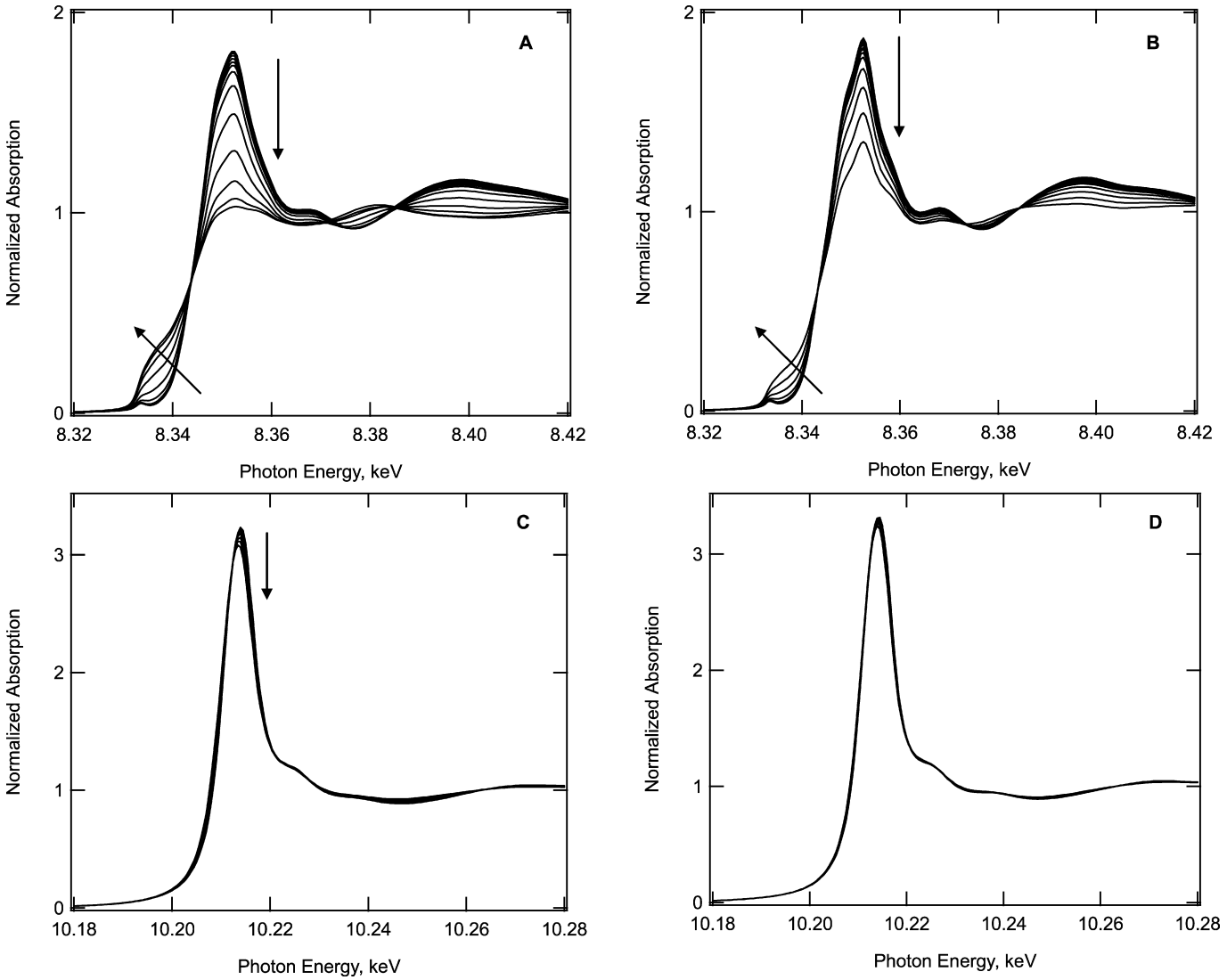

Fig. 3. In situ TPR XANES spectra of samples HCA and HCB as the catalyst is heated in hydrogen to 650 °C. Ni K-edge XANES for HCA (A), and HCB (B). W L_3-edge XANES for HCA (C) and HCB (D). There are 14 spectra shown in (A), 13 spectra in (B), 17 spectra in (C), and 19 spectra in D.

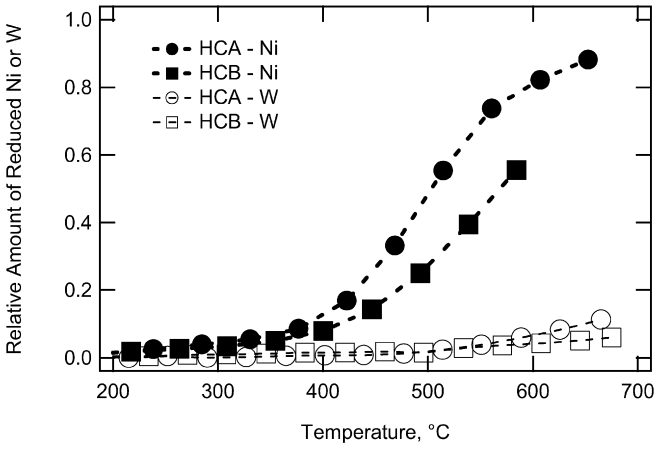

Fig. 4. Amount of reduced Ni and W relative to the total Ni or W in the two catalysts samples as a function of reduction temperature. The error of the fit is less than ±0.02 for each point.

TPR-XANES data with the bulk TPR data a clearer understanding of the metals reducibility is obtained and differences in the metals reducibility in different hydrocracking catalysts can readily be observed.

3.4. Structure of oxidized (calcined) catalysts

Representative TEM images of the oxidized catalysts are shown in Figs. 5A and 5B. It is difficult to visualize any discrete metal oxide particles in the images in either HCA or HCB, although some 7–10 Å W-rich particles are observed in HCA. Comparable particles are less frequently observed in the TEM images from HCB.

The Ni K-edge EXAFS spectra and models from the oxidized (and sulfided) HCA/B samples are shown in Fig. 6. The Fourier transformed Ni spectra and models from oxidized HCA/B samples are in Fig. 7. The EXAFS best-fit values for the Ni K-edge oxidized (and sulfided) HCA/B samples are listed in Table 5.

The Ni K-edge EXAFS spectra (Fig. 7) from the oxidized HCA/B samples are similar in phase and amplitude. Both spectra have maxima at 2, 4, 6, 8, and 9.5 $Å^{-1}$. Both spectra have the same decorations, such as shoulders at 2.5, 4.2, and 5.5 $Å^{-1}$, and a doublet at 8 $Å^{-1}$. The decorations of the oxidized HCB spectra are more pronounced than those of oxidized HCA spectra. The Fourier transform of the oxidized HCA/B spectra and model are shown in Fig. 7. As with the EXAFS $\chi(k)$ spectra, the magnitude of the Fourier transform is similar for both oxidized HCA and HCB spectra. Both spectra have well defined peaks at 1.8, 2.5, and

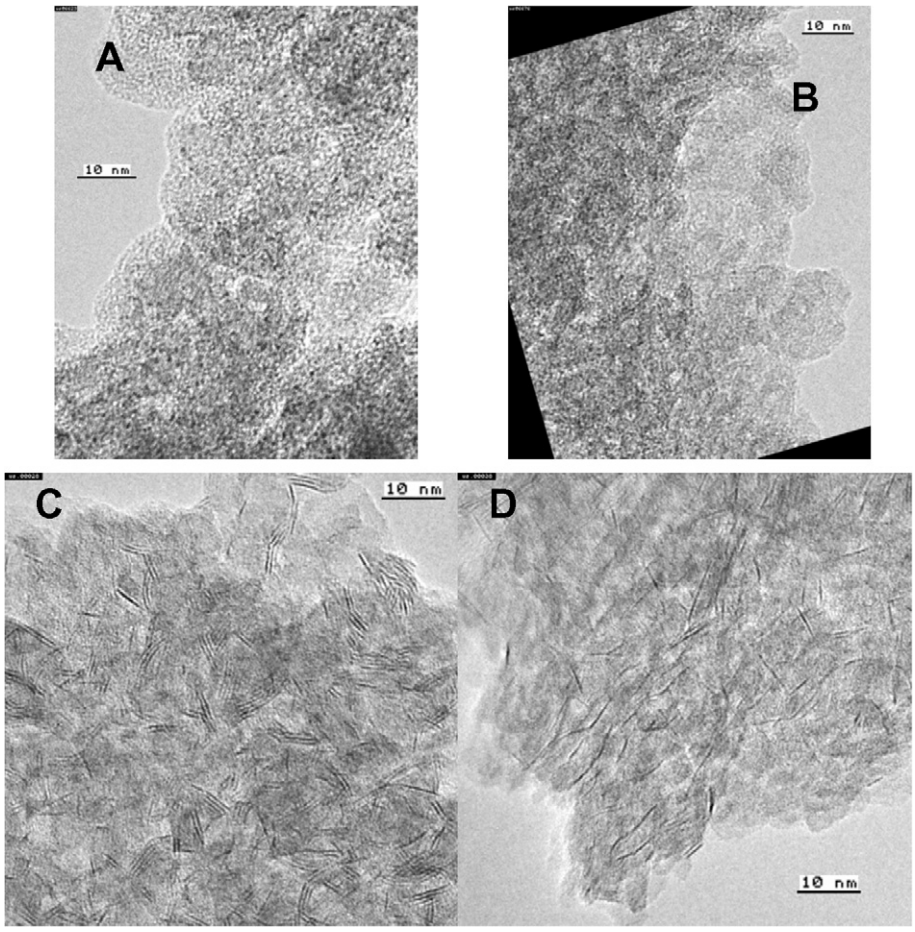

Fig. 5. TEM images of the oxidized catalysts (A and B) and the fully sulfided catalysts (C and D) for HCA and HCB, respectively. Small W-rich particles can be identified in HCA (A and B). These are less frequently observed in HCB. The dark thread-like features are the layers of WS_2 (C and D).

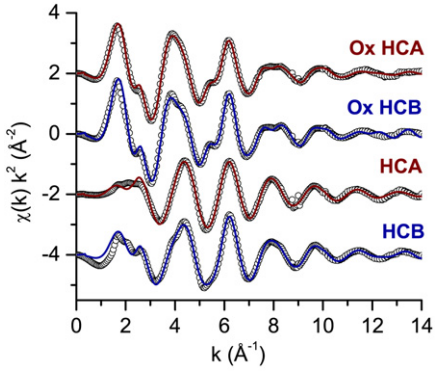

Fig. 6. Ni K-edge EXAFS spectra (symbols) and model (line) from oxidized and sulfided HCA/B samples.

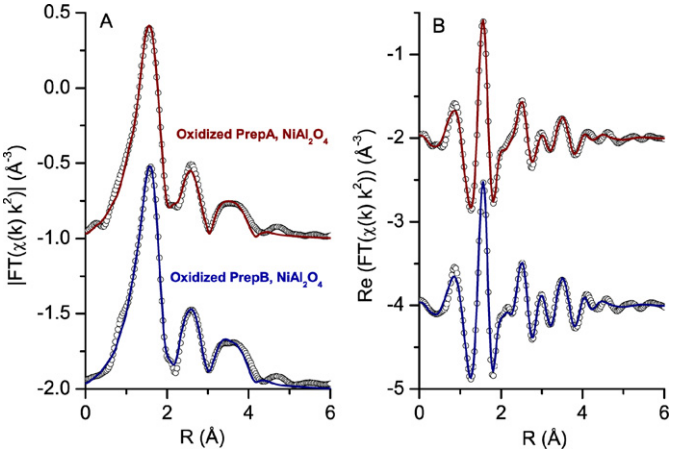

Fig. 7. Magnitude (A) and real part (B) of the Fourier transform of the Ni K-edge spectra (symbols) and model (line) based on the structure of octahedral Ni in $NiAl_2O_4$ from oxidized HCA sample (top) and from oxidized HCB sample (bottom).

3.5 Å. The real part of the FT (Fig. 7B) illustrates that the signal has a larger amplitude for HCB at 2.5, 3.0 and 3.5 Å. The differences in the oxidized HCA and HCB spectra are illustrated in the model fit parameters (Table 5) by an increase in the σ^2 values for HCA as compared to HCB. The σ^2 value for first oxygen shell is only slightly larger for HCA (0.0084 ± 0.0002 Å^2) than for HCB (0.0076 ± 0.0003 Å^2), while the σ^2 values of the more distant paths show a larger change in there best-fit values although there uncertainties are also larger. For example, the second Al path (Ni–Al_2) has a σ^2 value of 0.009 ± 0.002 Å^2 for HCB that increases to 0.013 ± 0001 Å^2 for HCA. The best-fit values for the path lengths are the same within the measurement uncertainties. The differences in the oxidized HCA and HCB spectra are consistent with a more disordered starting material in the HCA synthesis than that in the HCB synthesis. It is not thought that the oxidized Ni particle size changes substantially from HCA to HCB because the scattering path lengths are the same for both samples, and particle size affects usually occur with a decrease in the path lengths. In summary, the Ni K-edge spectra of oxidized HCA shows more disorder than the oxidized HCB spectra as demonstrated by the greater σ^2

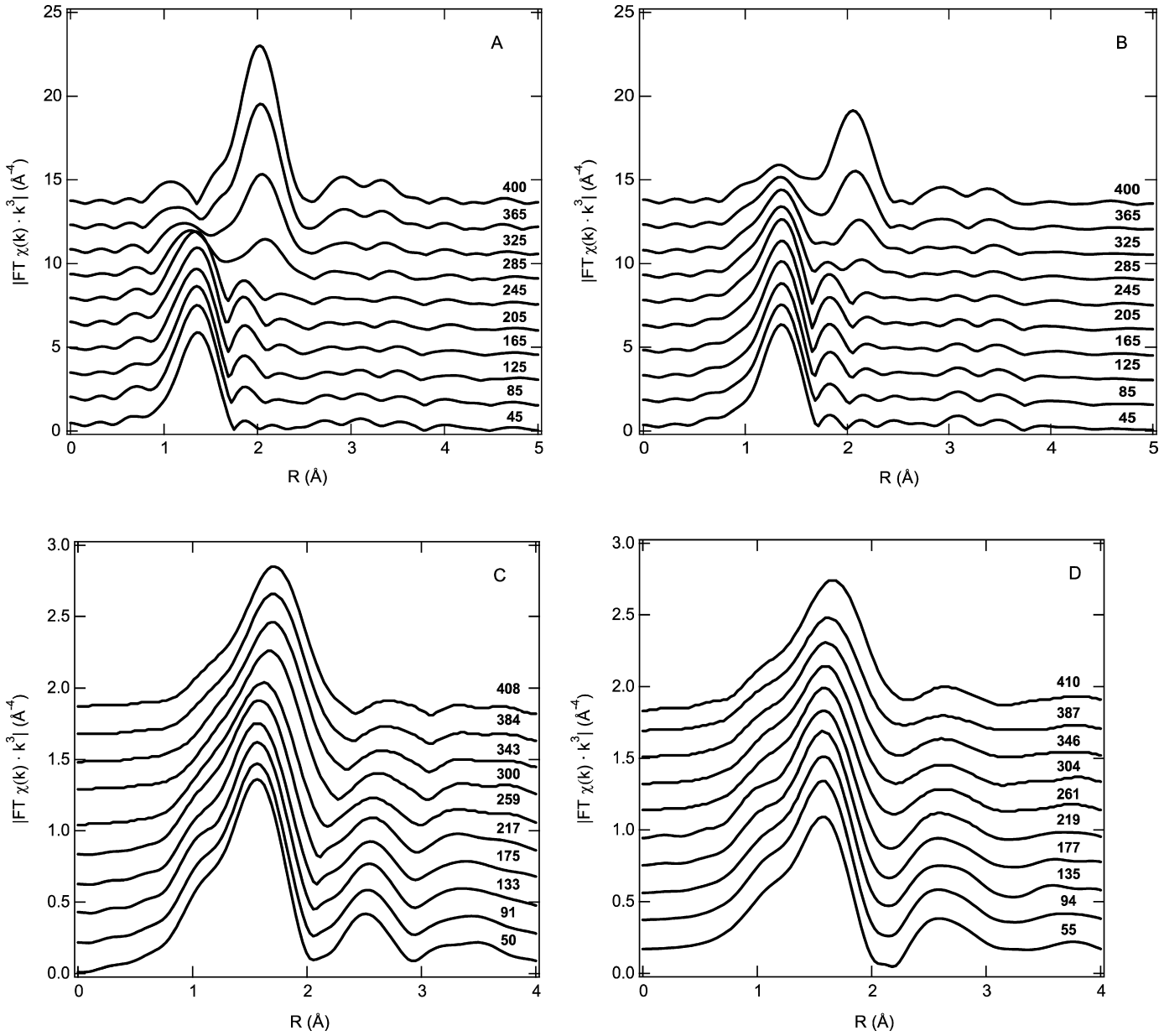

Fig. 8. The magnitude of the Fourier transform of the W L_3-edge (A and B) and the Ni K-edge (C and D) EXAFS spectra collected during in situ sulfidation of HCA (A and C) and HCB (B and D). The spectra have been offset by 1.5 for clarity. The temperature in °C during each scan is indicated on the figure.

values for HCA than for HCB (Table 5). This observation is consistent with the TEM data where well-defined metal-rich clusters are more prevalent in HCA.

3.5. Temperature programmed sulfidation: In situ XAFS

In situ W L_3-edge and Ni K-edge EXAFS and XANES data were collected during temperature programmed sulfidation. First, trends in the magnitude of the FT of the EXAFS spectra are compared, and then the XANES spectra are modeled using linear combination fitting. Figs. 8A and 8B show the $\chi(k)k^3$ FT of all the W L_3-edge EXAFS spectra collected during the in situ sulfidation of samples HCA and HCB, respectively. The first spectrum (bottom) is that of the calcined (oxidized) catalyst. The only observable peak in this initial spectrum is at 1.40 Å and is likely due to the contribution from the W–O bonds. The lack of a peak attributable to a neighboring W atom, which should be visible in the FT between 3.7 and 3.9 Å of the spectrum [40], is evidence for the high dispersion of the supported tungsten oxide species in the oxidized catalyst, in agreement with the TEM images (Fig. 5). The intensity of the first oxygen peak in the FT gradually decreases with increasing temperature in the flow of H_2S/H_2. This is a result of the oxidic tungsten being progressively sulfided. Note, however, that the intensity of this peak at any given temperature is always stronger in HCB than in HCA. The second major peak in the FT appears at a distance of ~2.0 Å. This is at the same distance as the first shell (W–S single scattering) of WS_2 (Table 1). Thus, the presence of this peak in the FT indicates the formation of W–S bonds that are likely from WS_2 platelets in the catalyst. This W–S signal first appears at about 285 °C in HCA, and at a higher temperature of 325 °C in HCB. A third, intermediate, peak is also evident in the W L_3-edge EXAFS spectra. This peak, at 1.9 Å, grows in intensity in both data sets, and then diminishes with increasing temperature. Previous studies have assigned this signal to an oxysulfide phase in which the first oxygen shell is partially replaced by sulfur atoms [9]. The presence of this intermediate phase is observable in both samples. Generally then the qualitative trends in these Fourier transforms

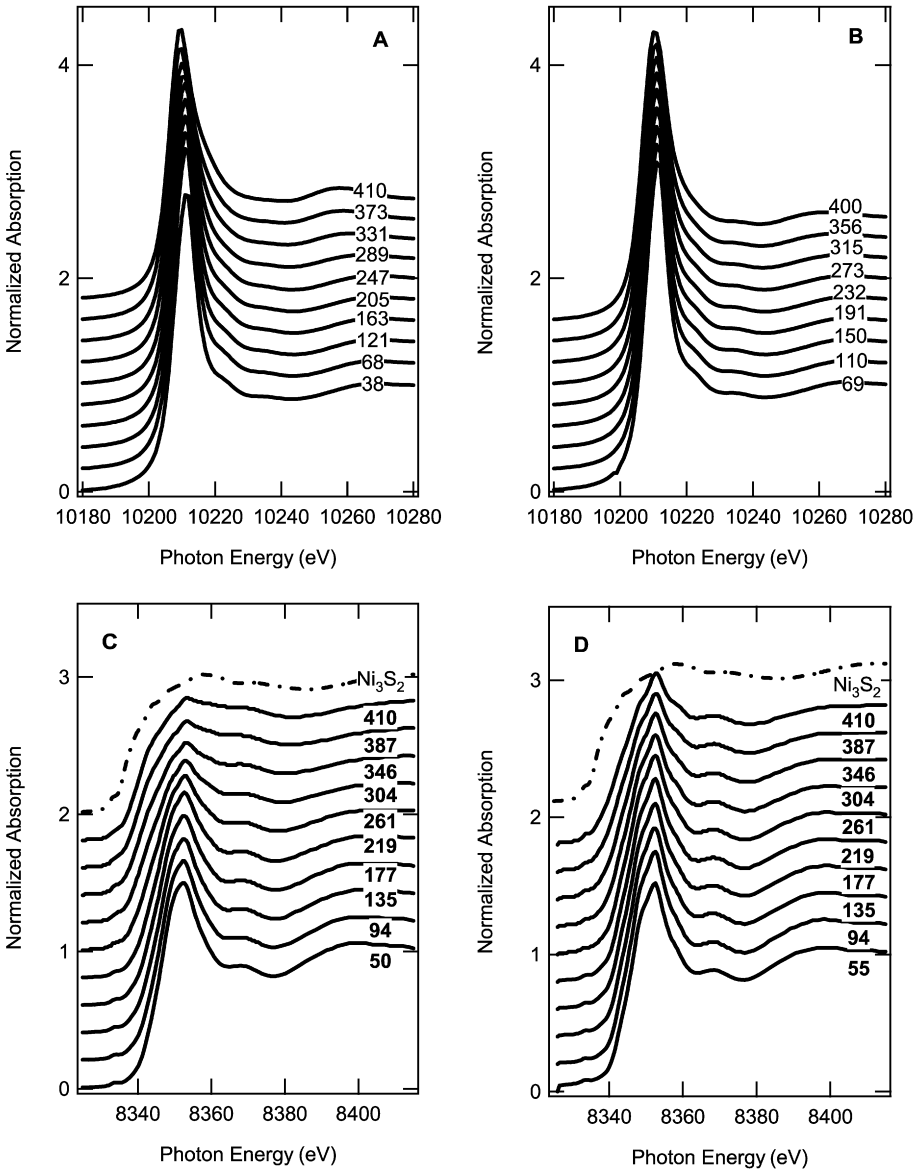

Fig. 9. XANES spectra of the W L_3-edge (A and B) and the Ni K-edge (C and D) during the in situ sulfidation of HCA (A and C) and HCB (B and D). The temperature recorded during each scan is indicated on the figure.

of the W L_3-edge EXAFS spectra show changes that can be interpreted within the chemistry of the system: As the tungsten oxide species in the catalyst becomes sulfided the first oxygen shell peak at 1.40 Å diminishes and the second W–S peak at 2.0 Å becomes more pronounced.

The magnitude of the FT's recorded during the in situ sulfidation at the Ni K-edge is shown in Figs. 8C and 8D. The first spectrum (bottom) is that of the oxidized catalyst, and shows a prominent peak at 1.56 Å that is assigned to neighboring O atoms. The change in the spectra with increasing temperature in the H_2S/H_2 (from bottom to top) is more subtle for the Ni EXAFS data compared to the W data. There is a shift in the peak to larger distance, with the first shell peak position gradually shifting from 1.56 to 1.67 Å at about 300 °C during the sulfidation of sample HCA. This same trend occurs for sample HCB, but at the substantially higher temperature of >350 °C. The peak shift corresponds to the difference in the bond distance typical for Ni–O (~2.1 Å) in the oxidized catalyst to the bond distance typical for Ni–S (~2.3 Å) in the sulfided catalyst. The shift is not as pronounced as in the W data as the change in average bond length between Ni–O and Ni–S is only <0.2 Å whereas in tungsten it is 0.58 Å.

While the spectral changes are more visually subtle in the Ni K-edge FT EXAFS data, they are in contrast quite striking in the Ni K-edge XANES data. Figs. 9C and 9D show the temperature programmed sulfidation XANES series of Ni K-edge spectra measured during the sulfidation of samples HCA and HCB, respectively. Here the oxidic nickel and sulfided nickel sulfide phases are easily distinguishable. Previous studies have shown that the white line of the Ni K-edge XANES is due to the ionic bonding between the nickel and oxygen [41,42]. As each oxygen atom is replaced by a sulfur atom, the white line intensity decreases due to the more covalent bond between nickel and sulfur [43,44]. In comparison the W L_3-edge XANES spectra acquired during in situ sulfidation are shown in Fig. 9A and 9B for HCA and HCB, respectively. The changes to the tungsten XANES spectra are more subtle compared to the Ni XANES spectra. This detailed comparison of the Ni and W XAFS data is a classic illustration of the relative merits of the XANES vs. EXAFS of each absorption edge

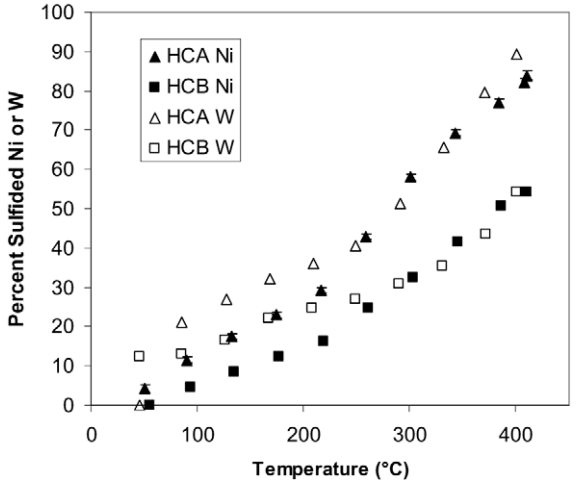

Fig. 10. The percentage of sulfided Ni and W as a function of temperature during the in situ sulfidation of HCA and HCB. The typical error bars are about the size of the symbols (illustrated on HCA Ni).

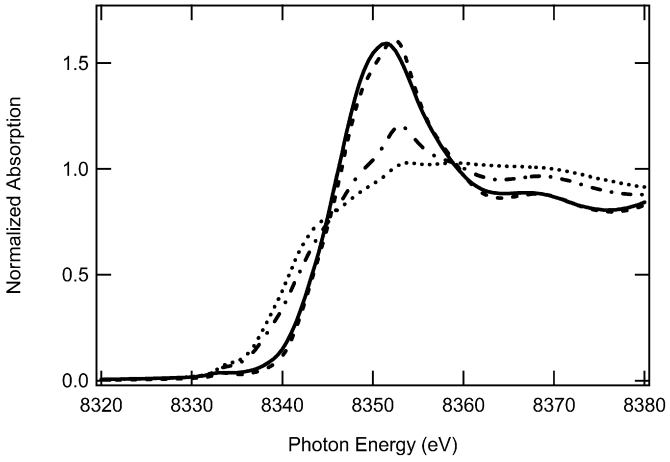

Fig. 11. XANES spectra comparison of the Ni K-edge for the oxidic and sulfided HCA (solid and dotted, respectively) and the oxidic and sulfided HCB (dashed and dot–dash, respectively).

as the species is transformed from oxidic to sulfidic in character.

The percentage of sulfidation of the Ni and W in each sample as a function of temperature is determined using a linear component fit to the XANES spectra. The resulting amount of the sulfidic component in each spectrum as a function of temperature is shown in Fig. 10. It can be seen that for the HCA sample, both the Ni and W are almost fully sulfided as the temperature reaches 410 °C (and indeed become fully sulfided after the extended hold at 410 °C). However, in sample HCB only about 50% of the Ni and W are sulfided as the temperature reached 410 °C. In both catalysts it appears that there is some excess sulfidation of the W relative to the Ni until around 250 °C, but thereafter the Ni and W sulfide simultaneously.

Fig. 11 shows the comparison of the XANES of the Ni K-edge for both the oxidic and final sulfided samples (after the 4 h dwell at 410 °C in the H_2S/H_2). The XANES spectra of the oxidic samples are subtly different (as are the EXAFS data, Section 3.5) although the exact origin of this difference have not been clarified. After the sulfidation the XANES spectrum of HCB has a stronger white line than that of HCA. This indicates that a larger fraction of the Ni in sample HCB remains unsulfided. The linear component fit indicates that in catalyst HCA the Ni was essentially fully sulfided whereas in catalyst HCB ~40% of the Ni remains unsulfided after the dwell at 410 °C. This amount is in excellent agreement with the number derived from the detailed EXAFS fitting (Section 3.6.2).

Table 4
Average sheet length and length weighted stacking number in the two catalysts.

Sample	Average length (nm)	Length weighted stack number
HCA	4.3 ± 1.4	2.8 ± 0.01
HCB	4.1 ± 1.4	1.4 ± 0.01

Table 5
Ni K-edge EXAFS best-fit values for sulfided HCA and HCB.

Path	Data set	CN	R (Å)	σ^2 ($\times 10^{-3}$ Å^2)	ΔE (eV)
		Paths for Ni–WS_2			
Ni–S_1	HCA	2.3 ± 0.56	2.209 ± 0.021	4.1 ± 1.9	0.35 ± 0.50
	HCB	1.4 ± 0.28	2.193 ± 0.017	2.1 ± 1.9	0.59 ± 0.66
		Paths for nanoparticulate Ni_2S_3			
Ni–S_1	HCA	0.54 ± 0.28	2.306 ± 0.014	4.1 ± 1.9	0.35 ± 0.50
	HCB	0.48 ± 0.12	2.293 ± 0.011	2.1 ± 1.9	0.59 ± 0.66
Ni–S_2	HCA	0.54 ± 0.28	2.345 ± 0.014	4.1 ± 1.9	0.35 ± 0.50
	HCB	0.48 ± 0.12	2.333 ± 0.011	2.1 ± 1.9	0.59 ± 0.66
Ni–Ni_1	HCA	0.54 ± 0.28	2.555 ± 0.015	15.2 ± 8.5	0.35 ± 0.50
	HCB	0.48 ± 0.12	2.541 ± 0.012	15.3 ± 6.1	0.59 ± 0.66
Ni–Ni_2	HCA	0.54 ± 0.28	2.592 ± 0.015	15.2 ± 8.5	0.35 ± 0.50
	HCB	0.48 ± 0.12	2.577 ± 0.012	15.3 ± 6.1	0.59 ± 0.66
		Paths for $NiAl_2O_4$[a]			
Ni–O_1	HCA	0.96 ± 0.18	2.028 ± 0.003	8.4 ± 0.2	0.35 ± 0.50
	HCB	2.46 ± 0.12	2.028 ± 0.005	7.6 ± 0.3	0.59 ± 0.66
Ni–Ni_1	HCA	0.48 ± 0.09	3.006 ± 0.022	12.7 ± 2.1	0.35 ± 0.50
	HCB	1.23 ± 0.06	3.042 ± 0.021	8.3 ± 3.5	0.59 ± 0.66
Ni-Al_1	HCA	0.48 ± 0.09	2.799 ± 0.059	37.3 ± 15.7	0.35 ± 0.50
	HCB	1.23 ± 0.06	2.788 ± 0.029	17.0 ± 5.5	0.59 ± 0.66
Ni-Al_2	HCA	0.96 ± 0.18	3.272 ± 0.012	12.5 ± 1.4	0.35 ± 0.50
	HCB	2.46 ± 0.12	3.259 ± 0.012	9.3 ± 1.9	0.59 ± 0.66
Ni–O_2	HCA	0.96 ± 0.18	3.178 ± 0.018	6.9 ± 3.3	0.35 ± 0.50
	HCB	2.46 ± 0.12	3.187 ± 0.018	1.9 ± 2.7	0.59 ± 0.66
Ni–O_3	HCA	1.92 ± 0.36	4.403 ± 0.011	27.1 ± 1.5	0.35 ± 0.50
	HCB	4.92 ± 0.24	4.397 ± 0.015	18.4 ± 1.6	0.59 ± 0.66
Ni–O_4	HCA	1.92 ± 0.36	4.472 ± 0.011	27.1 ± 1.5	0.35 ± 0.50
	HCB	4.92 ± 0.24	4.465 ± 0.015	18.4 ± 1.6	0.59 ± 0.66
Ni–Ni_2	HCA	0.96 ± 0.18	5.043 ± 0.016	19.2 ± 2.1	0.35 ± 0.50
	HCB	2.46 ± 0.12	5.023 ± 0.022	17.2 ± 3.0	0.59 ± 0.66

[a] Best-fit values for oxidized HCA and HCB are the same as for sulfided HCA and HCB, but with CN held at values determined by crystalline structure of $NiAl_2O_4$ (see Table 3).

3.6. Sulfided catalysts

3.6.1. Morphology: TEM

Representative TEM micrographs of the final sulfided HCA and HCB are shown in Figs. 5C and 5D, respectively. The black thread-like features indicate the WS_2 sheets for which the electron beam is tangential to the plane, the configuration giving by far the greatest observable contrast by TEM. A statistical analysis of the imaged particles was conducted from several TEM images, as described in the experimental section, to determine the average length of the WS_2 platelets, and the length weighted stack number. In all, 48 particles were averaged for HCB and 136 particles for HCA. The results of the analysis are given in Table 4. In both of the samples, the average length of the WS_2 sheets is similar and determined to be just over 4 nm. The maximum observed size of the WS_2 particles is ~8 nm in HCA and ~10 nm in HCB. However, the most distinct difference in the morphology of the WS_2 particles between the two samples is the length weighted stack number. There are far more single layers of WS_2 in HCB compared to multiple-layered WS_2 particles in HCA. This can clearly be seen by comparing Figs. 5C and 5D. Indeed, the length weighted stack number in HCA is 2.8 ± 0.01 while in HCB is 1.4 ± 0.01, confirm-

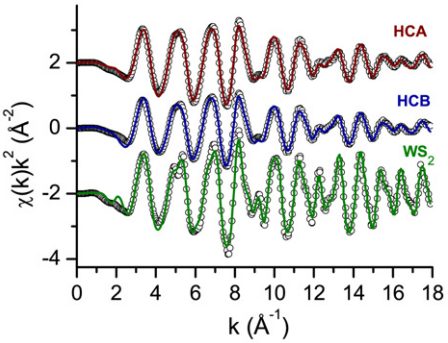

Fig. 12. W L_3-edge EXAFS spectra (symbols) and model (line) from sulfided HCA/B samples and also bulk WS_2.

ing the greater tendency for larger numbers of layers per particle to form in HCA than in HCB.

3.6.2. Structure determined by EXAFS

Fig. 12 shows the comparison of the W L_3-edge $\chi(k)k^2$ EXAFS of the catalysts HCA, HCB, and the WS_2 standard. The sulfided sample spectra are recorded at room temperature after 4 h at 410 °C in the flow of H_2S/H_2. The similarity of the WS_2 standard spectrum with the HCA and HCB spectra indicates a similar structure in the standard and sulfided samples. The overall amplitude of the EXAFS signal is stronger in HCA than in HCB. The amplitude of the EXAFS is determined by several factors: the degree of disorder (σ^2), the number of nearest neighbors (coordination number), and the atomic number of the scattering atom (Z). By applying these physical descriptions to the experimental W EXAFS data presented here it can be surmised that the reduced amplitude could be the result of one of the following reasons: (i) the WS_2 sheets are more uniform (σ^2), (ii) the lateral extent of the WS_2 platelets is larger (CN), or (iii) the amplitude is affected by the presence of unsulfided tungsten (Z = O vs. S).

The best-fit values for the W EXAFS models of HCA and HCB spectra are listed in Table 2, and the FT EXAFS spectra plotted in Fig. 13. Additional best-fit values are an energy shift (ΔE_0) of -3.8 ± 0.3 and -4.7 ± 0.3 for HCA and HCB, respectively. The fractional percentage of oxide component within HCB was determined to be $15 \pm 2\%$ while no significant oxide component was determined from the HCA spectra. The unit cell dimension, $a = b$, was determined to be 3.159 ± 0.003 Å and 3.158 ± 0.003 Å, for HCA and HCB, respectively. The fractional placement for S within the unit cell along the z-direction was found to be 0.1235 ± 0.0003 and 0.1238 ± 0.0003 for HCA and HCB, respectively. The resulting distances (R) for each path included in the model are listed in Table 2. These unit cell characteristics are consistent with the bulk WS_2 standard (Table 1) and with each other. The best-fit values for the CN are also consistent with each other but small relative the to WS_2 standard (Table 1). To compare the CN for the two catalyst samples, the coordination numbers for WS_2 of HCB are increased by 15% to account for the oxide component. For example, the first W–W1 neighbor CN for HCA is 3.6 ± 0.4 while for HCB is 3.7 ± 0.3 (3.2 ± 0.3 multiplied by 1.15). The measures of structural disorder (σ^2) values are almost identical with no clear trend in the determined values for HCA and HCB. The σ^2-values for HCA and HCB (Table 2) are almost double the values for the WS_2 standard (Table 1), indicating much more disorder in both the HCA and HCB structures as compared to the bulk WS_2.

The Ni K-edge EXAFS spectra and models from the sulfided HCA/B samples are shown in Fig. 6. The Fourier transformed spectra and models from the sulfided HCA/B samples are in Fig. 14. The EXAFS best-fit values for the Ni K-edge oxidized and sulfided HCA/B samples are listed in Table 5. The percentages of each Ni phase in the sulfided samples are listed in Table 6.

The Ni K-edge EXAFS spectra of the sulfided HCA and HCB samples (Fig. 6) are similar with maximum amplitudes at 2, 4, 6, 8, and 9.5 $Å^{-1}$. These spectra have fewer decorations than the oxidized spectra. An isolated Ni atom attached to the edge of the WS_2 sheet is expected to have little signal beyond the first shell which results in an EXAFS signal with fewer high frequency components (i.e. decorations). If the trends in the measured EXAFS spectra of the sulfided HCA and HCB as visually compared to the oxidized HCA and HCB spectra then the sulfided spectra are consistent with the formation of such monomeric sulfide species. The HCB spectrum retains some smaller versions of the decorations seen in the oxidized spectra, for example the shoulders at 2.4 and 5.8 $Å^{-1}$ and a broadening of the maximum at 8 $Å^{-1}$. The HCA spectrum is very smooth with little to no decorations. The Fourier transforms of the spectra for sulfided HCA and HCB are shown in Fig. 14. The FT of HCA spectrum is dominated by a single peak at 1.9 Å, while the HCB spectrum retains some structure similar to the oxidized spectra in the region from 3 to 5 Å.

The sulfided HCA and HCB spectra were modeled (the sulfided spectrum of each was modeled simultaneously with the respective calcined spectrum) with a combination of three distinct Ni-containing phases: oxidized Ni, nanoparticulate Ni_3S_2, and Ni decorating the edge sites of the WS_2. The $NiAl_2O_4$ phase represents

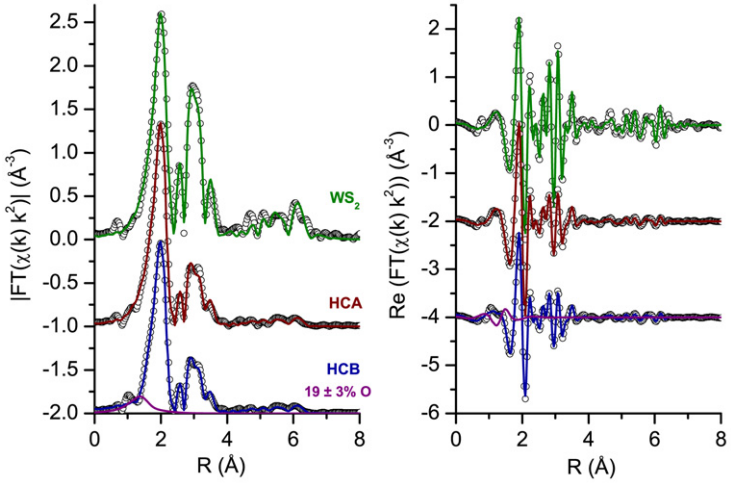

Fig. 13. Magnitude (left) and real part (right) of the Fourier transform of the W L_3-edge spectra (symbols) and model (line) from WS_2 (top row), sulfided HCA sample (middle row), and from sulfided HCB sample (bottom row). The W–O contribution ($15 \pm 2\%$) is shown for the HCB data.

Table 6
Percentage of Ni as Ni–WS_2, $NiAl_2O_4$, and nanoparticulate Ni_3S_2.

Phase	HCA	HCB
Ni–WS_2	58 ± 15%	35 ± 7%
Nanoparticulate Ni_3S_2	26 ± 15%	24 ± 7%
$NiAl_2O_4$	16 ± 3%	41 ± 2%

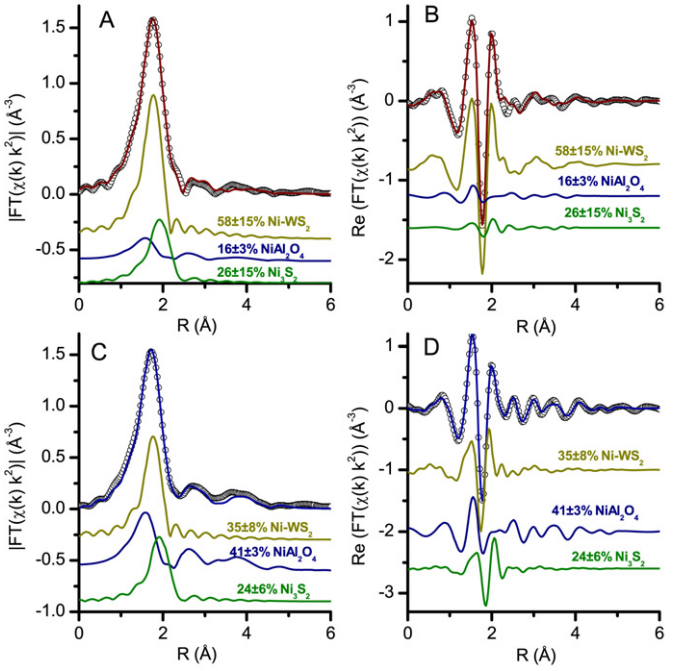

Fig. 14. Magnitude (A and C) and real part (B and D) of the Fourier transform of the Ni K-edge spectra (symbols) and model (line) from sulfided HCA sample (top row) and from sulfided HCB sample (bottom row). The three phase components of the model are shown offset beneath the measured spectra and model.

the oxidized catalyst. The Ni–WS_2 phase represents monomeric Ni tetrahedrally coordinated with S. This Ni is representative of the Ni decorating the edges of the WS_2 sheets. The Ni_3S_2 phase represents small clusters of tetrahedrally coordinated Ni that could also be decorating the edges of the WS_2 sheets or exist as a separate discrete phase on the support. (Thermodynamic conditions are appropriate for the formation of Ni_3S_2 [45]). These Ni_3S_2 clusters must be small because they are not detected in any of the TEM images. The percentages of these three phases in the sulfided HCA and HCB samples, as determined from this EXAFS model, are given in Table 6. The results indicate that the nanoparticulate Ni_3S_2 phase is similar in both HCA and HCB samples, supporting the hypothesis that this phase is formed by the relatively large concentration of mobile Ni during sulfidation, since both samples are sulfided under the same conditions and have the same concentration of Ni. The major difference in the Ni-containing phases of the sulfided catalysts is in the percentage of residual oxidized Ni (the $NiAl_2O_4$ component). The EXAFS modeling results indicate HCA has 16 ± 3% residual oxidized Ni while HCB has 41 ± 2% residual oxidized Ni. These percentages are robust with small uncertainties because of the extent of the EXAFS signal from the oxidized component in the model as shown in the Fourier transform from 3 to 5 Å (Fig. 14). Clearly the HCA catalyst has more sulfided Ni than the HCB catalyst. It is more difficult to accurately determine the relative fraction of monomeric Ni–WS_2 and nanoparticulate Ni_3S_2. These phases are structurally similar, and determining this relative fraction is particularly difficult for the HCA catalyst which has very little structure in the EXAFS signal beyond the first shell. This leads to relatively large uncertainties (15%) in the percentages of these two phases for the HCA catalyst. The spectrum from the HCB catalysis has a larger signal from the Ni–S bond of the nanoparticulate Ni_3S_2 phase leading to the smaller uncertainty of 7%. Even with these difficulties the fitting results indicate that the sulfided Ni in the HCB catalyst is evenly split between the Ni–WS_2 phase (35 ± 7%) and the nanoparticulate Ni_3S_2 phase (24 ± 7%) whereas for HCA there is more Ni–WS_2 phase (58 ± 15%) than nanoparticulate Ni_3S_2 (26 ± 15%). A simple two component linear combination fit to the respective Ni K-edge XANES data (Fig. S1) is also consistent with a significant difference in the amount of oxidized Ni in each of the catalysts. The relative amounts from the LCF XANES fit are: HCA 93 ± 1% sulfided, 7 ± 1% oxidized, and HCB 70 ± 1% sulfided, 30 ± 1% oxidized. These simplistic LCF values are in reasonable agreement with the EXAFS-derived values.

In summary the sulfided HCA catalyst has more sulfided Ni (combined Ni–WS_2 and nanoparticulate Ni_3S_2) than the sulfided HCB sample (84 ± 3% HCA vs. 59 ± 2% HCB), with indications of a difference in the relative amount of nanoparticulate Ni_3S_2 and Ni–W–S phase also.

4. Discussion

The characterization methodology described here provides a detailed description of the local structure of the Ni and W in fully-formulated hydrocracking catalysts, and provides information on the relative ease of sulfidation of the metals can be quantified. Moreover, using this detailed multi-shell EXAFS model, structural information on the relative amounts of three Ni-containing phases can be estimated.

Although the amount of the W and Ni in the two samples is the same, and both the composition of the support material and the calcination temperature of the two catalysts are identical, the different preparation methods result in different catalytic activity, different sulfidation behavior of the samples, and the extent of sulfidation. Regarding the activity differences there is always a measurable few degree offset in the activity, with HCB being less active than HCA.

A particularly striking fact is that all of the W and all of the Ni are fully sulfided in HCA after our in situ sulfidation conditions (4 h at 410 °C under atmospheric pressure of 10% H_2S/H_2). These results illustrate that it is possible to obtain essentially complete sulfidation of a Ni–W hydrocracking catalyst without fluoridation of the support or starting from partially sulfided precursors, in contrast to previous studies on alumina-only supported catalysts [8–12]. For example, on alumina-only supported catalysts of similar composition it is only in the case of catalysts prepared from ATT combined with fluoridation of the alumina does the degree of sulfidation approach completeness [8]. Clearly, then, in our study the ease of sulfidation of the Ni and W must be influenced by the presence of the other components in the catalyst formulation, the silico-aluminate components, in addition to the method of preparation of the catalyst. This raises an interesting question of the ability of being able to directly compare the equivalent characterization data from fully-formulated catalysts to the alumina-only supported (or carbon-supported) ones typically reported in the literature. The detailed mechanism, by which the individual components, the silico-aluminate and the alumina, affect the sulfidation of the Ni and W is, however, beyond the scope of this paper.

The overall sulfidation behavior of the two catalysts is somewhat similar, as can be seen from the analysis of the temperature programmed sulfidation XANES data (Fig. 10). The sulfidation of both the Ni and W begins below 100 °C and continues up to the final sulfidation temperature (410 °C). Below approximately 250 °C the sulfidation of the W is greater than that of the Ni, then above this temperature the sulfidation of the Ni and W for both prepa-

rations continues at the same rate. At any given temperature the sulfidation of HCA is greater than that of HCB.

At the end of the temperature ramp at 410 °C, almost all the W and all of the Ni in HCA are sulfided, whereas in HCB less than 50% of each is sulfided. It is thought that in order to achieve the highest activity catalyst (most promoter atom, Ni, decorating the step edges of the WS_2 phase) the tungsten should sulfide first and then the Ni to allow transport of the Ni to the step edges of the WS_2 [46]. In the HCA and HCB catalysts this is indeed observed up to 250 °C; the W sulfides before the Ni.

After the extended hold (4 h) at 410 °C in the HCA sample there is complete sulfidation of the W and almost complete sulfidation of the Ni (∼84% sulfidation), whereas in HCB there is both unsulfided W (∼15% unsulfided) and a significant amount of unsulfided Ni (∼41% unsulfided). The catalyst HCB has a degree of sulfidation that is typical of a more traditionally-prepared hydrocracking catalyst. We believe that the difference in the degree of sulfidation of the two catalysts is related to the degree of interaction of the Ni and W with the support: the method of preparation of HCB leads to a stronger interaction of the Ni and W with the support. This is also illustrated by the TPR, and TPR-XANES data, of the oxidized catalysts (Figs. 2–4) that show that the degree of reducibility of the metals differs considerably between the two catalysts. In HCA there is substantial reducible Ni (over 80% is reduced by 600 °C); while in HCB there is less reducible Ni (<60% at the same temperature). While in both catalysts there is little reduction of the tungsten there is some measurable reduction of the tungsten in HCA by 600 °C, whereas in HCB there is essentially no reduction by this temperature.

Thus, while at a macroscopic level there are similarities between the amount of reduction of the metals and the amount of sulfidation, which are indirectly related to the strength of interaction of the metals with the support, at a closer inspection it can be seen that it is not so simple. One might naively think that there would be a correlation in these two data sets; that the ease of sulfidation would be correlated with the ease of reduction. If this were true then TPR measurements could be used as a guide to the sulfidation behavior. However, there is no such obvious correlation. This fact is exemplified in particular for the tungsten. Up to 650 °C there is only a trace amount of reduction of the tungsten (Fig. 4), but at a substantially lower temperature (400 °C) the tungsten is essentially fully sulfided (Fig. 10). The specific details for this difference are beyond the scope of this paper, and have not been specifically addressed in the literature. Studies have been conducted on the reduction of the Ni and W, and studies on the sulfidation, but not ones comparing the two methods. This could be the subject of future work.

A difference in the degree of reducibility of Ni and W supported on alumina has been noted by, for example, Scheffer et al. [6]. In their TPR study they showed that the tungsten species did not begin reducing until around 700 °C, whereas the nickel species begin reducing at around 300 °C—both in substantial agreement with our work. More importantly they discussed that some of the Ni and W interacts strongly with the alumina to form discrete and distinct surface phases leading to the observation of strong interaction. For the nickel they concluded that some was incorporated into the surface layers to forms a surface nickel aluminate spinel, and some of the tungsten and nickel form a "NiWOAl" surface phase. While we have not studied the oxidized (calcined) form of the catalysts to any great extent there is evidence of a difference in the average local environment of the Ni (from XANES and EXAFS) and the W (from TEM) between the two catalysts. In the TEM images (Fig. 5) there are small W-rich particles in HCA, whereas in HCB there are far fewer of this type of particle. If indeed these particles are discrete tungsten oxide entities then the fact that fewer of them are observed in HCB suggests that the tungsten species must be more dispersed, and therefore on average interacting more strongly with the alumina (more W–O–Al bonds). For the nickel, there is a subtle difference in the Ni K-edge XANES (Fig. 11) and a measurable difference in the Ni EXAFS data (Fig. 6). In the Ni K-edge XANES the white line of the spectrum of HCB peaks at higher photon energy than that of HCA. The Ni K-edge XANES spectra of NiO and $NiAl_2O_4$ have previously been published [47] and this same energy shift is observed: that is, the white line maximum of nickel aluminate peaks at a higher energy than that of NiO. Moreover, in this prior study it was shown that the nickel on alumina is far less reducible when it is present as nickel aluminate. The analysis of the Ni EXAFS data show that the Ni is six-fold coordinated in the oxidized catalysts, and is consistent with all of the Ni being in a nickel aluminate type structure with the Ni occupying the octahedral sites in the spinel structure. Differences between the two preparations are somewhat subtle, and are manifested in the relative degree of disorder: HCA results in a more disordered Ni aluminate spinel than in HCB. It is likely that the Ni in the more ordered spinel in HCB would be more difficult to reduce. The EXAFS analysis of the Ni in the calcined catalysts is consistent with that expected for Ni both in a simple bulk spinel where it is known that Ni has a strong octahedral site preference [48] and also for a surface spinel where Ni also has preference for octahedral sites on the γ-alumina [49].

When all of these data are taken together the conclusion is reached that the method of preparation of HCB leads to a stronger interaction of both the Ni and the W with the support. This stronger interaction leads to the formation of surface phases (surface aluminates) that are both less reducible in hydrogen and less sulfidable in H_2S/H_2.

The nature of the tungsten oxysulfide phase that forms during the sulfidation has been the subject of several studies [8–12]. It is thought to be due to the partial initial substitution of the W–O bonds in the tungstate species with W–S bonds during the initial sulfidation before the tungsten is formally reduced from W(VI) to W(IV). This oxysulfide phase has been observed on both fluorided and non-fluorided alumina, and in the sulfidation of W/alumina and Ni–W/alumina. While the details of the formation of the oxysulfide phase are not the focus of this study it is clear that our in situ temperature programmed sulfidation EXAFS spectra (Fig. 8) are similar to those shown previously [8–12], and thus it is likely that a similar tungsten oxysulfide species is present, and is the intermediate between the oxidic tungsten species and the sulfided one. In both HCA and HCB the spectral features ascribed to the tungsten oxysulfide phase are observable almost immediately as the temperature ramp is initiated, and are substantially diminished by 250 °C. This general observation, and the temperature range over which the species is stable, is similar to these previous studies.

It is interesting to note that the sulfidation of the Ni and W occurs to a similar degree over the whole temperature range for both catalysts (Fig. 10). This suggests a strong correlation of the sulfidation of Ni and W. Such information is difficult to extract from standard temperature programmed sulfidation experiments, but becomes readily apparent from element specific structural characterization methods like XAS. However, such correlations are not always apparent. For example Sun et al. [9] show the sulfidation profiles for Ni in the different catalysts that they studied, but do not show the equivalent tungsten data. Our XAS data clearly show that even though there are structural differences in the initial oxidic W and Ni species the sulfidation of the Ni and W are strongly correlated. Such an experimental methodology is clearly essential for detailed studies aimed at elucidating the effect of various additives or methods of preparation on the sulfidation of the Ni and W in hydrocracking catalysts. Sun et al. state that Ni aids the sulfidation of the more-difficult-to-sulfide tungsten species.

Table 7
Summary of major fitting parameters from EXAFS studies of supported Ni–W catalysts.

Catalyst	W				Ni				Reference
	N_{W-S}	R_{W-S} (Å)	N_{W-W}	R_{W-W} (Å)	N_{Ni-S}	R_{Ni-S} (Å)	N_{Ni-W}	R_{Ni-W} (Å)	
Ni–W/SiO_2	4.3–6.7[a]	2.01–2.05	4.0–7.1	3.05–3.2	NR[b]	2.22[c]	NR	NR	[52]
Ni–W/C	6.4	2.41	4.5	3.14	4.0	2.21	1.5	2.78	[13]
					2.2	2.35			
Ni–W/C	6.4	2.41	4.4–4.5	3.14	4.0	2.21–2.23	1.1–1.5	2.78–2.80	[53]
					2.2–2.4	2.35–2.37			
Ni–W/Al_2O_3	NF[d]								[54]
Ni–W/Al_2O_3	1.0[e]	NR	1.0	NR	NR	NR	NR	NR	[22]
Ni–W/Al_2O_3	NF								[25]
Ni–W/Al_2O_3 SiO_2	NF								[55]
Ni–W/Al_2O_3	NF								[24]
Ni–W/Al_2O_3	NF								[10]
Ni–W/Al_2O_3	6.0[f]	2.41	6.0	3.16	NR	NR	NR	NR	[23]
Ni–W/Al_2O_3	1.75-2.47[g]	2.41–2.48	0.41–0.92	3.14–3.15	2.89[h]	2.21	NR	NR	[8]
					1.5	2.43			
Ni–W/Al_2O_3–F	4.35	2.41	2.30	3.15	2.06[h]	2.21	NR	NR	[8]
					2.63	2.36			
Ni–W/Al_2O_3 SiO_2	4.4–6.8	2.39–2.41	2.8–4.0	3.16–3.17	5.6	2.22	NR	NR	[29]
Ni–W/Al_2O_3 HCA	2.3 ± 0.6	2.21 ± 0.02	1.08 ± 0.56	$2.31–2.35 \pm 0.01$	5.7 ± 0.2	2.402 ± 0.002	3.6 ± 0.4	3.159 ± 0.003	This study
Ni–W/Al_2O_3 HCB[i]	1.4 ± 0.3	2.19 ± 0.02	0.96 ± 0.24	$2.29–2.33 \pm 0.01$	5.1 ± 0.1	2.400 ± 0.002	3.2 ± 0.3	3.158 ± 0.003	This study

[a] A range of values indicates different catalyst reported in the study.
[b] NR = not reported.
[c] From carbon-supported catalyst.
[d] NF = no fitting reported in study, only FT EXAFS spectra.
[e] Catalyst not fully sulfided.
[f] In fully sulfided sample. NW–S 3.4-4.6 and NW–W 2.9–3.2 in other samples in this study.
[g] A residual W–O contribution is also reported.
[h] A residual Ni–O contribution is identified in some catalysts. When a Ni–O contribution is reported in the fit only a single Ni–S distance is used at 2.14 Å.
[i] Ni–O CN of 1.2 ± 0.1 with bond length of 1.82 ± 0.02 Å.

It is now widely accepted that in Co–Mo hydrotreating catalysts the active phase is a "Co–Mo–S" phase where the cobalt atoms decorate the step edges of the MoS_2 sheets. A series of elegant model studies have clearly identified the location of these sites [50,51], and references therein. More recently, Lauritsen et al. [20] in an combined experiment/theory study using STM and DFT have expanded these model catalyst studies of to both Ni- and Co-promoted MoS_2 nanoclusters supported on Au(111). While the major structural features are similar between the two promoter atom types (the promoter atoms decorate the edge sites of the MoS_2 nanoclusters) there are differences in the details of the Ni-promoted compared to the Co-promoted ones. For the Ni-promoted structures they identified two types of structures, a Type A and a Type B. The Type A structures are associated with larger clusters (~2000 Å^2) with Ni substituting along the $(10\bar{1}0)$ edge (Mo edge, similar to Co–Mo–S), while Type B structures are smaller (<1000 Å^2), are dodecagonal in shape with Ni decorating three different edges. For each structure the special brim states are observed. These are metallic, one-dimensional edge states that are believed to be related to the unique catalytic activity of these structures [20]. A key conclusion from this work is that the Co or Ni is tetrahedrally coordinated to sulfur.

While there is relatively little fundamental (comparative model study) work on Ni–W hydrocracking catalysts, studies on γ-Al_2O_3-supported Ni–W catalysts are consistent with the active phase being similar to the Co–Mo–S model: the Ni decorates the step edges of the WS_2 sheets to form a Ni–W–S structure. For example, in a detailed EXAFS study of a fully sulfided carbon-supported Ni–W catalyst two Ni–S single scattering contributions are identified in the data [13]. These occur at distances of 2.22 and 2.35 Å, and were designated at Ni–S1 and Ni–S2, respectively. The four Ni–S1 sulfur atoms are those on the terminating edge face of a WS_2 sheet, while the two Ni–S2 sulfur atoms are sulfur atoms coordinated to the Ni projecting away from the face. Thus the overall Ni–S coordination number is six with the Ni in a distorted octahedral environment. This same split Ni–S shell was also used to fit the Ni EXAFS data from a γ-Al_2O_3 supported Ni–W catalyst [8]. Table 7 summarizes EXAFS data from the literature on Ni–W hydrocracking catalysts. In the majority of studies the EXAFS data are only used qualitatively.

In our study we modeled the Ni K-edge EXAFS data of the fully sulfided HCA and HCB catalysts. However, unlike the studies referenced in Table 7 three different Ni-containing phases were found to be necessary to adequately model the data. In both HCA and HCB catalysts there is residual unsulfided Ni. This was successfully modeled using Ni in the octahedral site in a spinel structure. For the sulfided Ni several different models were explored for the HCA sample as this has the smallest percentage of residual oxidized Ni.

First, a simple single shell fit was applied. This fit gave a Ni–S coordination number of 4.0 ± 0.4 at a bond length of 2.23 Å. This implies that whatever the final structure that is determined using a multi-shell fit the Ni has to be in a tetrahedral environment. The spectra could not be fit assuming 5 or 6-fold Ni–S coordination in a single shell, and are thus not consistent with [8,13]. This four fold CN and Ni–S bond length is consistent with the recent model study work for Co–Mo–S and Ni–Mo–S where the promoter atom is also found to be tetrahedrally coordinated [20], and also consistent with the crystal structure of Ni_3S_2 (heazelwoodite) where the Ni is in a distorted tetrahedral environment with two S (Ni–S1) at 2.285 Å and two S (Ni–S2) at 2.289 Å, followed by two Ni–Ni at 2.43 Å and two Ni at 2.53 Å.

Second, a split Ni–S shell was modeled in the same manner as the studies of Louwers at el. for Ni–W/C [13] and Schwartz et al. [8] for alumina-supported Ni–W. The model (4 Ni–S at 2.21 Å and 2 Ni–S at 2.35 Å) was found to be unstable and resulted in all of the sulfur atoms going to the same Ni–S distance. Thus, the data from the HCA sample are not consistent with the model determined by some other models. Instead our data are consistent with two different nickel sulfide species being present on the sulfided catalyst. First, a nanoparticulate Ni_3S_2 phase is used that is based on the structure of heazelwoodite with both Ni–S1 and Ni–S2 bond lengths and a Ni–Ni distance. Second, a site for Ni attached to a WS_2 cluster is used. This site, with Ni in a tetrahedral site with equidistant Ni–S bond lengths, is depicted in Fig. 1. This site is dif-

ferentiated [8,13] in that the Ni is binding to the $[10\bar{1}0]$ edge of the WS_2 compared to the $[\bar{1}010]$ edge (see also Ref. [56]).

Third, a model using only the nanoparticulate Ni_3S_2 phase and the oxidized Ni was used. This model did not work well: the Ni bound to the WS_2 is required. Fourth, a model using only the Ni attached to the WS_2 cluster and the oxidized Ni was used. Once again this model was statistically less accurate at describing the measured spectra as compared to using all three components as described in Section 2.4.2.

It is perhaps not surprising that in these catalysts the sulfided Ni is present as two distinct phases, a nanoparticulate Ni_3S_2 phase and the mono-atomic Ni species decorating the step edges of the WS_2 clusters, as the Ni/W ratio in these catalyst is 1:1, so there is an excess of Ni than would be needed to decorate the edges of all of the WS_2 clusters. However, for the Ni species promoting the WS_2 clusters our data are consistent with the mono-atomic Ni decorating the $[10\bar{1}0]$ edge of the WS_2 particles in a four-coordinated arrangement. Indeed, if the structure is examined a little more closely (Fig. 1) it can be envisaged that the sites where we believe the Ni to be promoting are the beginning of the nucleation of Ni_3S_2 clusters epitaxially growing out from the WS_2. From the Ni perspective a fully Ni-decorated edge of the WS_2 cluster begins to look like a single layer of Ni_3S_2.

Models of the W L_3-edge EXAFS data of the sulfided samples presented in this paper extends to 6.1 Å. In the layered structure of tungsten disulfide this relatively large distance (for EXAFS) only includes scattering paths within a single layer of the WS_2. The interlayer spacing of WS_2 is 6.18 Å, which is larger than the 6.0 Å of the measurable EXAFS signal. This means that the large signals within the EXAFS spectra do not help in determining the average number of layers in the WS_2 crystallites. The WS_2 structure has a layered morphology as can be seen in Fig. 1 and Fig. S2. The average number of layers within the small WS_2 particles of the catalyst is highly relevant to the performance of hydrocracking catalysts. Ideally the average number of layers in a small particle of WS_2 could be determined by the EXAFS data analysis. Unfortunately, the WS_2 structure has a relatively large interlayer spacing between the sheets (defined by the layers of W atoms) of approximately 6.18 Å. The hexagonal structure of the WS_2 sheets is offset with the S atoms directly above the W atoms of the next layer. From a W atom within one layer, the nearest neighbor within the next adjacent sheet is two sulfur atoms at a distance of 4.5 Å, followed by six tungsten atoms at a distance of 6.44 Å (denoted W4 within Fig. S2). The signal from the 2 S atoms at a distance of 4.5 Å was found to be insignificant in the bulk WS_2 spectrum. The signal from the six W4 atoms at a distance of 6.44 Å was detected but is in the same region of the spectrum as strong multiple scattering paths from the W–W1–W3 collinear atoms within the sheet structure (see Fig. S2). Therefore it is difficult to determine the average number of layers of the WS_2 structure based on the EXAFS data. Therefore complementary techniques such as TEM are needed to determine the structures defined by distances greater than 6.0 Å–in this study the number of layers in the WS_2 platelets. The TEM analysis shows a clear distinction in the average number of layers between the two catalysts, with particles on average having twice the number of layers in HCA compared to HCB (Table 4). It is tempting to hypothesize that the catalyst that had the most dispersed tungsten in the oxidized form (HCB) resulted in a catalyst with the more dispersed tungsten in the sulfided form. This is clearly a simplistic explanation, but the mobility of the partially reduced tungsten species on the support surface may play a role in the final morphology of the WS_2 particles. Another possible explanation is that the kinetics of the sulfidation of the W and/or the Ni is different in the two catalysts. In the first case, the initial formation of WS_2 in HCB is observed at a higher temperature than in HCA. This may be due to the lower mobility of the W on the surface due to the stronger interaction of the oxide to the support. In either scenario, the WS_2 forms at a higher temperature in HCB and, for the same dwell time, less WS_2 particles would merge together resulting in most of the WS_2 remaining in a single layer. In the second case, the Ni promotes the sulfidation of the W and that this results in multiple layers. It has been shown that incorporation of Ni into the tungsten-only catalysts increases the fraction of the WS_2 with a higher average stacking, and with smaller crystal size [11]. In our case, since much more of the Ni in HCB is tied up in the support as a surface aluminate and is not sulfidable, the promotion effect is severely reduced. This then would lead to a greater fraction of single WS_2 layers as found in HCB compared to HCA.

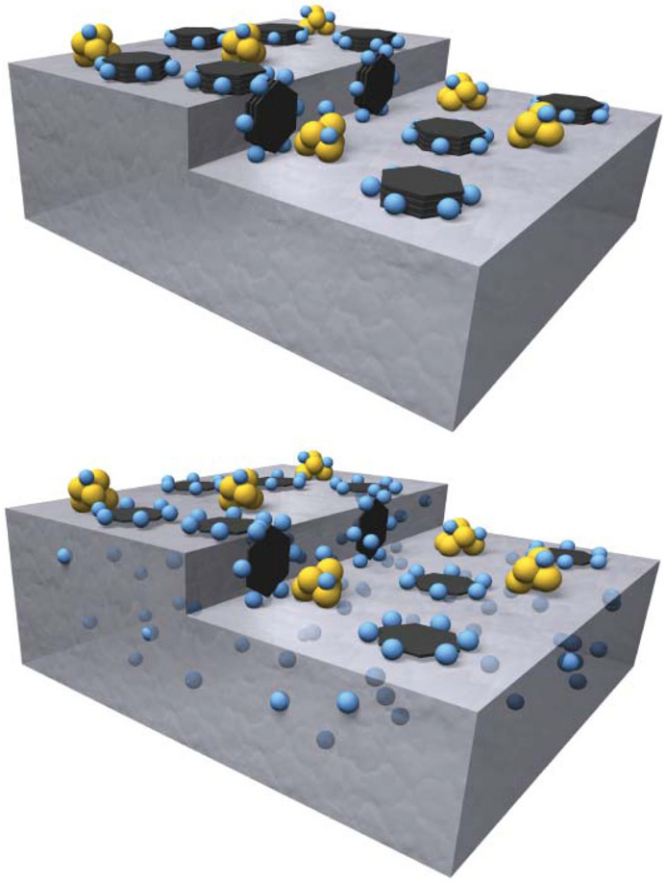

Fig. 15. Schematic models of the sulfided catalysts in HCA (top) and HCB (bottom). The black hexagons represent the WS_2 sheets, the blue spheres Ni atoms, and the yellow and blue clusters the clusters of Ni_3S_2. Clearly the exact shape of the WS_2 clusters is not known, and are depicted as hexagons given the morphology of bulk WS_2.

A schematic representation of the Ni and W structures that are believed to be present on both the sulfided HCA and HCB catalysts is depicted in Fig. 15. The illustration shows the single and multiple layered WS_2 particles, together with the three Ni phases.

The average size of the WS_2 particles should be obtainable from the coordination numbers determined from the EXAFS analysis. This is a result of the finite size of the particles imposing a reduced average coordination number from the bulk values. However, it has been reported that for small supported MoS_2 particles there is a discrepancy between the average lateral extent measured by TEM and that determined by EXAFS [26]. For these hydrotreating catalysts the average size of the MoS_2 layers was determined to be 20-44 Å by TEM and only about 10 Å by EXAFS. The explanation forwarded by Shido and Prins for this apparent discrepancy was that the MoS_2 particles are highly disordered and distorted [26].

This therefore results in deviations from the ideal lattice positions, especially for the critical Mo–Mo single scattering distance. If these distortions are taken into account then, by the use of a modified calibration curve of CN of the Mo–Mo versus diameter of the MoS_2 particle, it was shown that the EXAFS data now agree with the TEM data. The authors do qualify their model with the statement that other effects, such as curvature of the layers, defects, and site disorder may also be factors. If the calibration curve of Shido and Prins is applied to the average W–W coordination number for HCA (CN 3.6 ± 0.4), then a particle diameter of around 3.5 nm is obtained. This is in reasonable agreement with the TEM-measured value (Table 4) of ca. 4.3 ± 1.4 nm. The small discrepancy between the two measurements is possibly the result of a difference in the degree of order of WS_2 particles. This mosaic spread in geometric values would result in a weaker EXAFS signal. This would be very difficult to verify by TEM since the TEM can only show the contrast from the layers parallel to the electron beam. As a result, the mosaic structure cannot be seen from the TEM picture and it appears that the single layers have the same length as the multiple layers. A second possibility is that TEM undercounts the number of small platelets, especially those present as single layers [21]. A 3-D electron tomography study [19] could possibly resolve this issue.

5. Conclusions

Fully formulated (γ-Al_2O_3/alumino-silicate) Ni–W hydrocracking catalysts were prepared by two different methods, HCA and HCB. These catalysts contained the same wt% of metals, the same wt% of the different constituents, and were calcined at the same temperature prior to the sulfidation. The sulfidation of tungsten and nickel in these samples was followed using time resolved in situ XAFS at both the Ni K-edge and W L_3-edge. The two sulfided catalysts exhibit different catalytic activity, with HCA being more active than HCB.

In the oxidized (calcined) catalysts the metals are well-dispersed on the support, with the degree of dispersion greater in HCB. The Ni in each formulation is six-fold coordinate and present as a nickel aluminate-type species.

A clear picture emerged of the sulfidation behavior of the two samples. In both catalysts the sulfided tungsten phase exists as nanoclusters of WS_2 but there is a clear difference in the average number of WS_2 layers in the clusters: on average the platelets contain twice as many layers in HCA compared to HCB. There may also be a slight difference in the average cluster size of the WS_2 nanoclusters between the samples. The comparative study shows that in one catalyst (HCA) the W is fully sulfided whereas in HCB about 15% of the W remains oxidic at the end of the 410 °C sulfidation condition.

The Ni in the sulfided form of both preparations is present as three distinct phases: Ni that remains oxidized and is not sulfided under our conditions, a nanocluster Ni_3S_2 phase, and a monoatomic Ni phase that decorates the edges sites of the WS_2 clusters. There is a large difference in the amount of the Ni that is sulfided at the end of the 410 °C sulfidation condition for the two preparations. In HCA ~84% of the Ni is sulfided whereas in HCB only about 60% of the Ni is sulfided. Moreover, there is also evidence for a difference in the relative amount of the Ni_3S_2 and Ni–W–S phase in the two samples. In all cases the Ni is present as four-fold coordinate with sulfur.

Both catalysts appear to go through the same tungsten oxysulfide intermediate during the sulfidation and the sulfidation of the Ni and the W occurs simultaneously above 250 °C.

It is hypothesized that some of the structural differences in the sulfided phase are related to structural differences observed in the oxidized catalyst: more of the Ni and W interacts more strongly with the alumina, and is well-dispersed in HCB compared to HCA. It is likely that the activity differences are related to these morphological differences.

Acknowledgments

Karl Steigleder, Suheil Abdo, and Li Wang are thanked for many stimulating discussions, and Sue Tonnesen is thanked for the TPR data. Use of the Advanced Photon Source was supported by the US Department of Energy, Office of Science, Office of Basic Energy Sciences, under Contract No. W-31-109-Eng-38.

Supplementary material

The online version of this article contains additional supplementary material.

Please visit DOI: 10.1016/j.jcat.2009.01.019.

References

[1] S.P. Ahuja, M.L. Derrien, J.F. Le Page, Ind. Eng. Chem. Prod. Res. Develop. 9 (1970) 272.
[2] T. Kabe, W.H. Qian, A. Funato, Y. Okoshi, A. Ishihara, Phys. Chem. Chem. Phys. 1 (1999) 921–927.
[3] A. Stanislaus, B.H. Cooper, Catal. Rev. Sci. Eng. 36 (1994) 75.
[4] M. Breysse, M. Cattenot, T. Decamp, R. Frety, C. Gachet, M. Lacroix, C. Leclerq, L. de Mourgues, J.L. Portefaix, M. Vrinat, M. Hourari, J. Grimblot, S. Kaszelan, J.P. Bonnelle, S. Housni, J. Bachelier, J.C. Duchet, Catal. Today 4 (1988) 39.
[5] K.T. Ng, D.M. Hercules, J. Phys. Chem. 80 (1976) 2094.
[6] B. Scheffer, P.J. Mangnus, J.A. Moulijn, J. Catal. 121 (1990) 18.
[7] H.R. Reinhoudt, A.D. van Langeveld, P.J. Kooyman, R.M. Stockmann, R. Prins, H.W. Zandbergen, J.A. Moulijn, J. Catal. 179 (1998) 443.
[8] V. Schwartz, M.Y. Sun, R. Prins, J. Phys. Chem. B 106 (2002) 2597–2605.
[9] M.Y. Sun, T. Burgi, R. Cattaneo, R. Prins, J. Catal. 197 (2001) 172–181.
[10] M.Y. Sun, T. Burgi, R. Cattaneo, D. van Langeveld, R. Prins, J. Catal. 201 (2001) 258–269.
[11] M.Y. Sun, P.J. Kooyman, R. Prins, J. Catal. 206 (2002) 368–375.
[12] M.Y. Sun, D. Nicosia, R. Prins, Catal. Today 86 (2003) 173–189.
[13] S.P.A. Louwers, R. Prins, J. Catal. 139 (1993) 525.
[14] A. Benitez, J. Ramirez, A. Vazquez, D. Acosta, A. Lopez Agudo, Appl. Catal. A 133 (1995) 103.
[15] E. Payen, R. Hubaut, S. Kasztelan, O. Poulet, J. Grimblot, J. Catal. 147 (1994) 123.
[16] J. Ramirez, P. Castillo, A. Benitez, A. Vazquez, D. Acosta, A. Lopez Agudo, J. Catal. 158 (1996) 181.
[17] J.V. Sanders, J.R. Anderson, M. Boudart (Eds.), Catalysis Science and Technology, Springer-Verlag, Berlin, 1985, p. 51.
[18] L. Vradman, M.V. Landau, Catal. Lett. 77 (2001) 47–54.
[19] K.P. de Jong, L.C.A. van den Oetelaar, E.T.C. Vogt, S. Eijsbouts, A.J. Koster, H. Friedrich, P.E. de Jongh, J. Phys. Chem. B 110 (2006) 10209–10212.
[20] J.V. Lauritsen, J. Kibsgaard, G.H. Olesen, P.G. Moses, B. Hinnemann, S. Helveg, J.K. Norskov, B.S. Clausen, H. Topsoe, E. Laegsgaard, F. Besenbacher, J. Catal. 249 (2007) 220–233.
[21] M.P. De la Rosa, S. Texier, G. Berhault, A. Camacho, M.J. Yacaman, A. Mehta, S. Fuentes, J.A. Montoya, F. Murrieta, R.R. Chianelli, J. Catal. 225 (2004) 288–299.
[22] T. Kameoka, H. Yanase, A. Nishijima, T. Sato, Y. Yoshimura, H. Shimada, N. Matsubayashi, Appl. Catal. A 123 (1995) 217.
[23] M.J. Vissenberg, Y. van der Meer, E.J.M. Hensen, V.H.J. de Beer, A.M. van der Kraan, R.A. van Santen, J.A.R. van Veen, J. Catal. 198 (2001) 151–163.
[24] H. Yasuda, M. Higo, S. Yoshitomi, T. Sato, M. Imamura, H. Matsubayashi, H. Shimada, A. Nishijima, Y. Yoshimura, Catal. Today 39 (1997) 77–87.
[25] Y. Yoshimura, T. Sato, H. Shimada, N. Matsubayashi, M. Imamura, A. Nishijima, M. Higo, S. Yoshitomi, Catal. Today 29 (1996) 221.
[26] T. Shido, R. Prins, J. Phys. Chem. B 102 (1998) 8426–8435.
[27] H.R. Reinhoudt, E. Crezee, A.D. van Langeveld, P.J. Kooyman, J.A.R. van Veen, J.A. Moulijn, J. Catal. 196 (2000) 315–329.
[28] G. Kishan, V.H. Coulier, V.H. de Beer, J.A.R. van Veen, J.W. Niemantsverdriet, J. Catal. 196 (2000) 180–189.
[29] Y. van der Meer, E.J.M. Hensen, J.A.R. van Veen, A.M. van der Kraan, J. Catal. 228 (2004) 433–446.
[30] S.R. Bare, G.E. Mickelson, F.S. Modica, A.Z. Ringwelski, N. Yang, Rev. Sci. Instrum. 77 (2006).
[31] B. Ravel, M. Newville, J. Synchrotron Rad. 12 (2005) 537–541.
[32] M. Newville, J. Synchrotron Rad. 8 (2001) 322–324.
[33] E.A. Stern, M. Newville, B. Ravel, Y. Yacoby, D. Haskel, Physica B 208 (1995) 11.
[34] J.J. Rehr, R.C. Albers, Rev. Mod. Phys. 72 (2000) 621–654.
[35] V.L. Kalikhman, Neorg. Mater. 19 (1983) 1060.
[36] H. Fjellvag, A. Anderson, Acta Chem. Scand. 48 (1994) 290–293.

[37] R.W.G. Wycoff, Crystal Structures, R.E. Krieger Publishing, Malabar, 1982, p. 251.
[38] C.A. Otero, J.S.D. Vinuela, J. Solid State Chem. 60 (1985) 1.
[39] L. Brillouin, Science and Information Theory, Academic Press, New York, 1967.
[40] A.J. van der Vlies, R. Prins, T. Weber, J. Phys. Chem. B 106 (2002) 9277–9285.
[41] R. Cattaneo, T. Shido, R. Prins, in: Hydrotreatment Hydrocracking of Oil Fracture, in: Studies in Surface Science and Catalysis, vol. 127, 1999, pp. 421–425.
[42] F.W. Lytle, R.B. Greegor, A.J. Panson, Phys. Rev. B 37 (1998) 1550.
[43] S.P.A. Louwers, M.W.J. Craje, A.M. Vanderkraan, C. Geantet, R. Prins, J. Catal. 144 (1993) 579–596.
[44] F.W. Lytle, P.S.P. Wei, R.B. Greegor, G.H. Via, J.H. Sinfelt, J. Chem. Phys. 70 (1979) 4849–4855.
[45] T. Rosenqvist, J. Iron Steel Ins. 176 (1954) 37.
[46] G. Kishan, J.A.R. van Veen, J.W. Niemantsverdriet, Top. Catal. 29 (2004) 103–110.
[47] S.R. Bare, F.S. Modica, A.Z. Ringwelski, J. Synchrotron Rad. 6 (1999) 436–438.
[48] A. Navrotsky, O.J. Kleppa, J. Inorg. Nucl. Chem. 29 (1967) 2701.
[49] M. Lo Jacono, M. Schiavello, A. Cimino, J. Phys. Chem. 75 (1971) 1044.
[50] J. Kibsgaard, J.V. Lauritsen, E. Laegsgaard, B.S. Clausen, H. Topsoe, F. Besenbacher, J. Am. Chem. Soc. 128 (2006) 13950–13958.
[51] H. Topsoe, B.S. Clausen, F.E. Massoth, in: A. Anderson, M. Boudart (Eds.), Catalysis: Science and Technology, Springer-Verlag, Berlin, 1996.
[52] D.I. Kochubei, M.A. Kozlov, K.I. Zamaraev, V.A. Burmistrov, A.N. Startev, Y.I. Yermakov, J. Appl. Catal. 14 (1985) 1.
[53] S.P.A. Louwers, M.W.J. Graje, A.M. van der Kraan, C. Geantet, J. Catal. 144 (1993) 579.
[54] N. Matsubayashi, T. Sato, H. Shimada, M. Imamura, Y. Yoshimura, A. Nishijima, T. Kameoka, K. Masuda, in: J.A. Pajares, J.M.D. Tascon (Eds.), Coal Science, Elsevier, 1995, p. 1495.
[55] H. Makishima, Y. Tanaka, Y. Kato, S. Kure, H. Shimada, N. Matsubayashi, A. Nishijima, M. Nomura, Catal. Today 29 (1996) 267.
[56] S.P.A. Louwers, R. Prins, J. Catal. 133 (1992) 94–111.